

# SceneTok: A Compressed, Diffusable Token Space for 3D Scenes

Mohammad Asim Christopher Wewer<sup>†</sup> Jan Eric Lenssen

Max Planck Institute for Informatics, Saarland Informatics Campus

{masim, cwewer, jlenssen}@mpi-inf.mpg.de

<sup>†</sup> Corresponding author

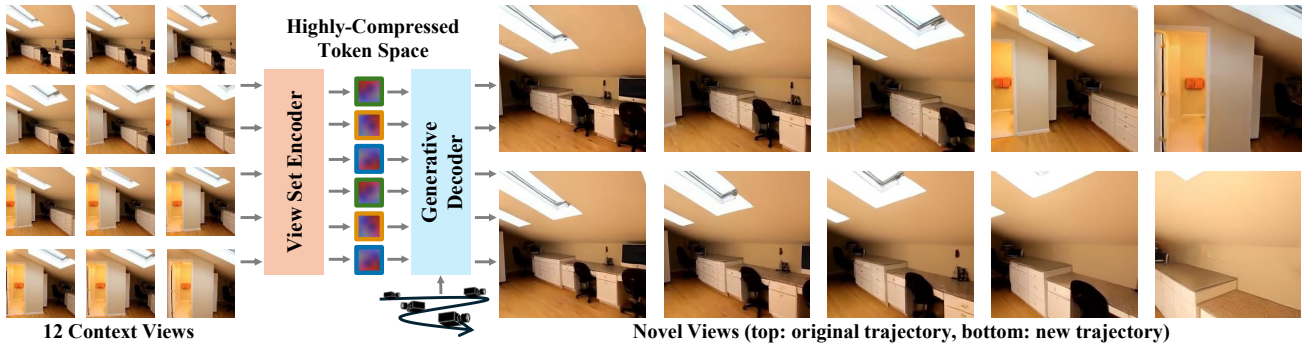


Figure 1. **Setup Overview.** We introduce SceneTok, a tokenizer that encodes view sets into an unstructured, highly-compressed set of tokens, which can be efficiently rendered (32 images per second) from novel trajectories with a light-weight generative decoder. The token space is diffusible and allows latent generation of scenes in 8 seconds.

## Abstract

We present SceneTok, a novel tokenizer for encoding view sets of scenes into a compressed and diffusible set of unstructured tokens. Existing approaches for 3D scene representation and generation commonly use 3D data structures or view-aligned fields. In contrast, we introduce the first method that encodes scene information into a small set of permutation-invariant tokens that is disentangled from the spatial grid. The scene tokens are predicted by a multi-view tokenizer given many context views and rendered into novel views by employing a light-weight rectified flow decoder. We show that the compression is 1-3 orders of magnitude stronger than for other representations while still reaching state-of-the-art reconstruction quality. Further, our representation can be rendered from novel trajectories, including ones deviating from the input trajectory, and we show that the decoder gracefully handles uncertainty. Finally, the highly-compressed set of unstructured latent scene tokens enables simple and efficient scene generation in 5 seconds, achieving a much better quality-speed trade-off than previous paradigms. Code is available online: [geometric-rl.mpi-inf.mpg.de/scenetok/](https://geometric-rl.mpi-inf.mpg.de/scenetok/)

## 1. Introduction

Answering the question of how to best represent 3D scenes in the era of large-scale, multi-modal, generative models

is one of the most pressing research milestones for several applications in computer vision and graphics, such as reconstruction [4, 9, 18, 19, 22, 32, 33, 54, 62, 67, 73], open-world scene understanding [17, 35, 66], reasoning [7, 11, 29, 55], or generation of 3D worlds [3, 13, 44, 46–48, 60, 70, 71]. Such representations come with several requirements: (1) being trainable from a data source that is available in vast quantities, like videos, (2) being simple in structure to expose an easy interface to large-scale, potentially multi-modal generative models, (3) being highly compressive to handle the large-scale nature of 3D scenes. In this work, we make an important step towards this goal by introducing SceneTok, an autoencoder that encodes 3D scenes from videos into a set of unstructured, highly compressed tokens, which can be rendered from novel views and can be processed by generative diffusion models to perform conditional generation in latent space.

Existing paradigms for 3D scene generation often use an underlying 3D data structure [3, 47, 48, 60] or posed multi-view images and videos [13, 44, 46, 65, 71]. The former has several limitations. Due to the lack of 3D data and the cubic scale of 3D-structured representations, training of large foundation models is prohibitively expensive or impossible. The latter enables generative modeling by learning from large-scale video data. However, these models are typically large and require specialized sampling strategies such as

history-guided and autoregressive generation [6, 44] or anchored generation [13, 44, 46, 65, 71] to produce large and consistent scenes; therefore, they necessitate immense computing effort due to the simultaneous generation of coarse structures and rendered details. Recent works in generalizable 3D reconstruction [18, 19, 42, 43] encode images into a simplified latent space that is disentangled from the spatial grid. However, they have been shown to perform only view interpolation [33], i.e., they cannot be rendered from novel views, and due to high dimensionality, these methods do not enable generation or other downstream tasks.

In contrast, `SceneTok` employs a simple 2-stage approach. In the first stage, we train an autoencoder to compress a given set of context views into an unstructured set of continuous tokens. The representation can subsequently be decoded by a lightweight, diffusion-based renderer, sampling multiple novel views in less than a second, and accounting for the remaining uncertainty in the scene representation. To show the usefulness of our latent space, we introduce a second stage, which consists of a diffusion model trained on the scene token space from stage one, enabling view-conditioned generation. The cascaded approach changes the generative paradigm from view-space to a compressed latent-space and *decouples view rendering from scene generation*. This allows allocating more resources to the generative model, i.e., scaling it up without affecting the rendering speed. Furthermore, the compressed space makes it highly efficient to perform generation.

We evaluate both stages independently and show that `SceneTok` achieves state-of-the-art reconstruction quality, can render novel trajectories, and can gracefully resolve uncertainty in the scene representation. Decoding is efficient, allowing the rendering of 32 novel views in 1 second on an Nvidia RTX 4090. Meanwhile, our latent diffusion model on the obtained representation can effectively perform conditional 3D scene generation in 5 seconds, which is orders of magnitude faster than other scene generation paradigms. In summary, we propose:

- a novel paradigm for scene generation that decouples *view rendering* from *generation*.
- a compressed, unstructured token representation for scenes that enables fast *rendering* from novel views using a scene autoencoder (`SceneTok`) that encodes and decodes a set of posed views of a scene to and from a compressed token set with a generative renderer.
- a diffusion transformer model (`SceneGen`) that performs *generation* in the latent space very efficiently.

## 2. Related Work

`SceneTok` is a 3D scene tokenizer for efficient generation. It can be seen at the intersection of vision tokenizers for latent image and video generation (cf. Sec. 2.1), 3D scene reconstruction (c.f. Sec. 2.2), and generation (c.f. Sec. 2.3).

### 2.1. Vision Tokenizers for Latent Generation

Scalable and efficient image and video generation with autoregressive transformers [36] or diffusion models [16] relies on autoencoders, also known as vision tokenizers, that compress data into compact latent spaces.

**Spatial Autoencoders.** Pioneering works VQGAN [12] and Latent Diffusion [41] leverage 2D convolutional autoencoders for spatial perceptual compression of images into discrete codebook indices or continuous latents, respectively. In both cases, the latent space maintains the 2D image structure but in a lower resolution. This paradigm has been successfully extended to 3D convolutional tokenizers for videos [38, 57, 69]. Moreover, recent follow-up works improve this family of autoencoders in terms of stronger compression [8] and "diffusability" of the latent space [59].

**1D Tokenizers.** Another new line of research proposes to encode images [2, 53, 63] and videos [51] into unstructured token sets or 1D sequences. These are directly compatible with autoregressive generation, whereas 2D or 3D patch tokens for images and videos lack an intuitive order.

With `SceneTok`, we propose the first tokenizer that compresses 3D scenes into an unstructured token set. While grid-like representations from spatial autoencoders are computationally feasible for images and videos, the cubic cost of voxel grids severely limits scalability.

### 2.2. Feed-Forward 3D Scene Reconstruction

A feed-forward 3D reconstruction pipeline can be seen as an autoencoder that encodes a set of input views and reconstructs a set of target views. An important design choice is the intermediate representation encoding the 3D scene.

**Explicit Representation.** Several works encode input views into 3D Gaussians [4, 9, 10, 54, 56, 67, 73] and NeRFs [5, 20, 52, 61] by directly predicting them in a feed-forward manner. However, both NeRFs and 3D Gaussians have large representation sizes that are high-dimensional in nature and thus follow a complex distribution, making them ill-suited for efficient and scalable generation.

**Latent Representation.** Closer to our method are LVSM [19] and RayZer [18], which do not impose any 3D inductive bias but predict novel views directly using large-scale transformer architectures. However, both leverage more than 3K high-dimensional ( $\geq 512$ ) tokens which makes latent diffusion on their representations infeasible. Moreover, in addition to information leakage in RayZer [18], concurrent work shows that it lacks transferability [33], i.e., the ability to synthesize novel views that deviate from the original input camera trajectory.

In contrast, `SceneTok` is the first 3D scene tokenizer that produces a highly compressed representation, well-suited for generation via latent diffusion and allows for transferable novel view synthesis.

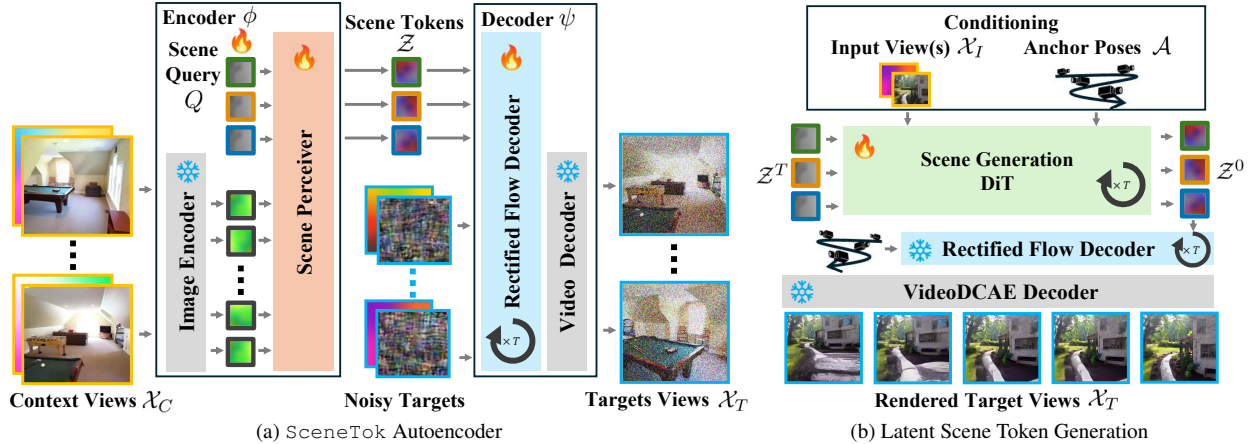


Figure 2. **Method Overview.** (a) The SceneTok autoencoder encodes view sets into a set of compressed, unstructured scene tokens by chaining a VA-VAE image compressor and a perceiver module. The tokens can be rendered from novel views with a generative decoder based on rectified flows. (b) A latent diffusion transformer can perform scene generation by generating compressed scene tokens. Scene generation can be conditioned on a single or a few images and a set of anchor poses, defining the spatial scene extent.

### 2.3. Generative Models for 3D Scenes

Scene generation has largely evolved from optimization-based 3D to feed-forward view-space generation, with the availability of large-scale video and multi-view datasets facilitating state-of-the-art generation performance.

**Generation in 3D-Space.** Several works [21, 26, 28, 34, 40, 48] allow direct generation of 3D representations, either via Score-Distillation-Sampling (SDS) or by baking 3D representations into the architecture. This results in 3D consistent generation [1]; however, they are not scalable with the size of the scene and are mostly limited to object-centric scenes. Overall, the training and inference of such models require immense computational effort and resources, while large-scale 3D datasets remain very limited.

**Generation in View-Space.** Conditional multi-view [13, 71] and video [44, 65] diffusion models generate target views directly conditioned on input view(s). While they can leverage the availability of large-scale datasets for pre-training, rendering novel views still requires expensive generation steps, as the models are typically large to ensure good generation quality. However, the entanglement of view rendering with generation causes redundancies, e.g., when revisiting the same views that were previously generated, resulting in a waste of computing resources.

In this work, we leverage the benefits of both worlds: (1) the disentanglement of *rendering* and *generation*, and (2) utilizing large-scale multi-view and video data. Additionally, we can allocate more capacity towards generation and enable fast rendering with a lightweight decoder.

## 3. SceneTok

The core of our method is an autoencoder (c.f. Fig. 2a), which takes a set of  $N$  context images  $\mathcal{X}_C = \{\mathbf{x}_i\}_{i=1}^N$  as ob-

servations of a 3D scene with camera poses  $\mathcal{P}_C = \{\mathbf{p}_i\}_{i=1}^N$  and encodes them via the encoder  $\phi$ , i.e.

$$\mathcal{Z} := \{\mathbf{z}_i\}_{i=1}^K = \phi(\mathcal{X}_C, \mathcal{P}_C), \quad (1)$$

where  $\{\mathbf{z}_i \in \mathbb{R}^d\}_{i=1}^K$  is a set of continuous tokens. Then, a decoder  $\psi$  takes tokens  $\mathcal{Z}$  and a novel camera trajectory  $\mathcal{P}_T := \{\mathbf{p}_i\}_{i=1}^M$  and renders it, i.e.

$$\mathcal{X}_T = \psi(\mathcal{Z}, \mathcal{P}_T), \quad (2)$$

where  $\mathcal{X}_T := (\mathbf{x}_i)_{i=1}^M$  is a sequence of  $M$  novel views for the given camera poses, which can be supervised (during autoencoder training), or serve as output during inference. In the second stage, we formulate a generative model on the token set  $\mathcal{Z}$  (c.f. Fig. 2b). We will introduce the encoder in Sec. 3.1, the decoder in Sec. 3.2, the training in Sec. 3.3, and the latent generative model in Sec. 3.4.

### 3.1. Encoding the Scene

SceneTok predicts an unstructured set of tokens  $\mathcal{Z} := \{\mathbf{z}_i\}_{i=1}^K$  as the output of the encoder  $\phi$ , which forms our latent scene representation. During encoding, we first compress each image  $\mathbf{x}_i \in \mathbb{R}^{H \times W \times 3}$  into a latent feature map  $\mathbf{f}_i \in \mathbb{R}^{\frac{H}{16} \times \frac{W}{16} \times 32}$  using the VA-VAE encoder [59] with 16x spatial compression. These features from all views  $\mathcal{F}_C := \{\mathbf{f}_i\}_{i=1}^N$  are fed as  $1 \times 1$  latent patch tokens into a dedicated branch of the following scene perceiver. Inside each block, camera poses  $\mathcal{P}_C$  are transformed into ray maps  $\mathcal{R}_C = \{\mathbf{r}_i \in \mathbb{R}^6\}_{i=1}^N$  with  $\mathbf{r}_i = [\mathbf{o}_i, \mathbf{d}_i]$  for ray origins  $\mathbf{o}_i$  and directions  $\mathbf{d}_i$ , which are used to modulate the corresponding patch tokens via AdaLN [37] before a multi-view attention layer and an MLP.

A second branch of the perceiver, dedicated to the scene tokens, processes a set of directly optimized scene queries  $Q := \{q_i\}_{i=1}^K$  with  $q_i \in \mathbb{R}^{d_H}$  (c.f. Fig. 3). Each block of

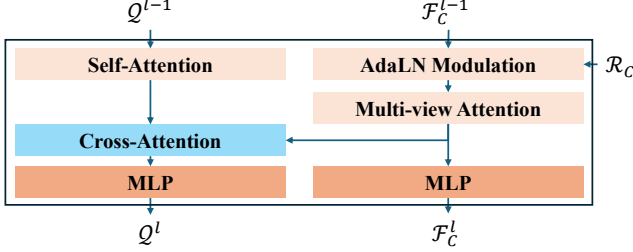


Figure 3. **A single scene perceiver block.** The scene perceiver module consists of  $L$  blocks, alternating self-attention between scene queries  $\mathbf{Q}$  and cross-attention to the multi-view encoder branch, which is AdaLN-modulated with ray embeddings.

this branch consists of self-attention and cross-attention to the intermediate multi-view patch tokens of the first branch. Figure 3 shows an individual encoder block with  $\mathcal{F}_C^0 = \mathcal{X}_C$  and  $\mathcal{Q}^0 = \mathcal{Q}$ . We obtain the scene tokens  $\mathcal{Z}$  after an additional projection to a lower dimension  $d$ . We provide hyperparameter and architectural details in Appendix Sec. A.

**Choice of Positional Encoding.** Each visual token from the context views is encoded using rotary positional encodings (RoPE) [45]. We found that invariances defined by positional encodings strongly influence the scene representation. 3D RoPE [30], as is common in video encoders, gives the context views a temporal order perceivable by the encoder and leads to an unwanted temporal bias. Thus, we employ only 2D RoPE, which leads to an order invariant encoder and ensures that the scene tokens can be rendered from arbitrary trajectories later. More details and findings are provided in Appendix Sec. C.

### 3.2. Decoding the Scene

A scene representation can lack information about details that are necessary to render certain novel views in sufficient quality. In `SceneTok`, there are two common sources of uncertainty: (1) information that is already missing from the input views, or (2) high-frequency details that are lost due to compression. Both lead to varying uncertainty when rendering novel views, depending on the specific view. We find that it is crucial to resolve this uncertainty via sampling, which requires a generative renderer  $\psi$  to decode the representation  $\mathcal{Z}$  by sampling from a conditional distribution  $p_\psi(\mathbf{x}|\mathcal{Z})$ . Note that the renderer can also adapt to varying uncertainty based on location. For regions that are clearly defined by the scene tokens, it can learn to sample from a narrow distribution while falling back to pure generation in cases of high uncertainty. In Figure 6, we show that there is a correlation between the variance of rendered outputs and the information in the tokens.

**Decoder Architecture.** We implement the rendering function  $\psi$  as a two-step procedure. During inference, we first employ a rectified flow generator  $\Psi$  that iteratively denoises latent image patches for novel trajectories, according

to a reverse process from  $\mathbf{x}^1$  to  $\mathbf{x}^0$ . One step of the denoising process computes

$$\mathbf{x}^{t-\Delta t} = \mathbf{x}^t - \Delta t \Psi(\mathbf{x}^t, \mathcal{R}, \mathcal{Z}, t), \quad (3)$$

conditioned on  $t$ , ray maps  $\mathcal{R}$  of a novel trajectory, and scene tokens  $\mathcal{Z}$ , where  $\mathbf{x}^1$  is initialized from a standard Gaussian distribution and  $\Delta t$  is the step size. We use flow-parameterization for rectified flow, predicting a vector field (c.f. Sec. 3.3). The resulting  $\mathbf{x}^0$  are decoded into pixel space by the VideoDCAE [38] decoder from Open-Sora 2.0.

Our diffusion network is a diffusion transformer model and closely resembles that of LightningDiT [59]. We remove class conditioning and instead condition each latent token on its corresponding ray map token by merging it with the timestep embedding [44] and applying AdaLN, as in Sec. 3.1. In each block, we condition on the scene tokens  $\mathcal{Z}$  via a cross-attention layer. We employ latent-space diffusion over pixel space due to its efficiency, which is essential for the fast rendering of scene tokens via conditional generation with a video diffusion model. We provide further discussions and technical details in Appendix Sec. A.

### 3.3. Training

We keep the VA-VAE encoder and VideoDCAE decoder frozen while training the rest of the architecture end-to-end with the rectified flow matching objective [24, 27] in latent space. Specifically, for each output view, the output of the decoder is a vector field, i.e.

$$\mathbf{v}^t = \Psi(\mathbf{x}^t, \mathcal{R}, \mathcal{Z}, t). \quad (4)$$

Then, the objective function is a simple MSE between the ground truth flow  $\mathbf{x}^1 - \mathbf{x}^0$  and the predicted flow:

$$\mathcal{L}(\psi) = \mathbb{E}_{t, \mathbf{x}^1, \mathbf{x}^0} \|\mathbf{x}^1 - \mathbf{x}^0 - \mathbf{v}^t\|_2^2, \quad (5)$$

where  $\mathbf{x}^t = t\mathbf{x}^1 + (1-t)\mathbf{x}^0$ ,  $\mathbf{x}^1 \sim N(\mathbf{0}, \mathbf{I})$ , and  $\mathbf{x}^0$  are latent target images from the training set. When training end-to-end (i.e., when  $\mathcal{Z}$  is parameterized by the encoder  $\phi$ ), we effectively learn to extract a representation  $\mathcal{Z}$  from the observations  $\mathcal{X}_C$  and  $\mathcal{P}_C$  that maximizes the likelihood of rendering our target views. Meanwhile, the decoder can learn to adapt to varying conditioning strength from  $\mathcal{Z}$ . See Sec. 4.2 and 4.4 for further analysis on the  $\mathcal{Z}$ .

### 3.4. Latent Scene Generation

Once we trained the autoencoder, we can freeze both the encoder and decoder and train a simple diffusion transformer [58] to model the conditional distribution  $p(\mathcal{Z}|\mathcal{X}_I, \mathcal{A})$  over the scene tokens  $\mathcal{Z}$  with  $\mathcal{A} := \{\mathbf{a}_i \in \mathbb{R}^6\}_{i=1}^N$  being camera anchors and  $\mathcal{X}_I$  a single or a few conditioning image(s). A single anchor is defined as  $\mathbf{a}_i = [\mathbf{o}_i, \mathbf{d}_i]$ , where  $\mathbf{o}_i, \mathbf{d}_i \in \mathbb{R}^3$  are the  $i^{\text{th}}$  position and viewing direction of a camera in 3D space. We embed

	12 Context Views						5 Context Views					
	Repr. Size (#Floats)	PSNR $\uparrow$	LPIPS $\downarrow$	SSIM $\uparrow$	rFVD $\downarrow$	rFID $\downarrow$	Repr. Size (#Floats)	PSNR $\uparrow$	LPIPS $\downarrow$	SSIM $\uparrow$	rFVD $\downarrow$	rFID $\downarrow$
<i>Explicit Representation</i>												
MVSplat [9]	46.40M	20.13	0.255	0.755	354.46	29.89	19.33M	22.82	0.152	0.856	144.91	15.85
MVSplat360 [10]	74.71M	21.09	0.247	0.769	294.82	25.64	31.12M	23.88	0.174	0.828	136.52	18.15
DepthSplat [56]	46.40M	21.55	0.202	0.809	204.52	21.35	19.33M	24.45	0.124	0.884	109.74	12.89
<i>Latent Representation</i>												
LVSM [19]	1.57M	21.25	0.262	0.686	211.66	26.40	1.57M	25.74	0.140	<b>0.831</b>	111.14	13.37
<b>SceneTok</b>	<b>32.76K</b>	<b>23.99</b>	<b>0.159</b>	<b>0.783</b>	<b>79.80</b>	<b>11.12</b>	<b>32.76K</b>	<b>25.97</b>	<b>0.133</b>	0.817	<b>76.24</b>	<b>11.26</b>

Table 1. **Quantitative comparison of NVS quality on RE10K.** SceneTok achieves superior performance compared to previous works achieving significant improvements in terms of rFVD and rFID alongside with PSNR and LPIPS while having a significantly smaller representation size.

the ray map and take a single averaged embedding over all pixel to minimize the number of tokens. The complete set  $\mathcal{A}$  defines the spatial extent and layout of the scene that is to be generated. Conditioning on such anchors allows us to control how much the scene tokens must span and helps define the camera trajectories for rendering novel views later. Because we center our scenes around the origin during encoding (c.f. Sec. 3.1), we can always set the first input image and the anchor to the scene origin and set the rotation to the identity. The subsequent camera poses for the anchors, input, and target views are provided relative to this origin. The scene generation transformer, which we denote as SceneGen in the experiments, is also trained using rectified flows (c.f. Eq. 5) on a dataset of encoded scene tokens. We provide training details in Sec. 4.1.

## 4. Experiments

In this section, we devise a set of experiments that showcase the potential of our method. We choose baselines that solve novel view synthesis and scene generation with different paradigms and aim to answer the following questions:

- Q1:** How does the SceneTok autoencoder fare against prior works in terms of novel view synthesis quality?
- Q2:** Do the scene tokens satisfy the properties of a 3D representation, i.e., allow rendering from novel trajectories?
- Q3:** Does the compressed token representation allow for efficient scene generation in latent space and how does it compare against multi-view and video generators?

We define our experimental setup in Sec. 4.1, answer Q1 and Q2 in Sec. 4.2, and finally Q3 in Sec. 4.3.

### 4.1. Experimental Setup

We devise a series of experiments to evaluate the novel-view synthesis quality and transferability [33] of SceneTok on novel trajectories, as well as the single-view generation quality of SceneGen.

**Baselines.** We evaluate SceneTok, MVSplat [9], MVSplat360 [10], DepthSplat [56], Long-LRM [73], RayZer [18], and LVSM [19] on novel-view synthesis. Note that we mainly compare our method against LVSM, as it employs a latent representation. Although RayZer

also employs a latent representation, it uses target views as inputs, unlike SceneTok and LVSM, which results in information leakage (c.f. Sec. 2.2 and 4.2). For scene generation, we provide fair comparisons against RealEstate10K baselines, including DFM [48], a 3D diffusion model with an underlying NeRF representation, and a video diffusion model DFoT [44]. We also compare against SEVA [71], which is trained on a large corpus of closed-source data.

**Dataset.** We train and test on RealEstate10K [72], DL3DV [23], and further experiment with zero-shot generalizability on ACID [25]. For RealEstate10K, we evaluate in two settings where we select: (1) 270 scenes, each with 5 context and 64 target views, which we define as the narrow-view baseline; (2) 136 scenes, each with 12 context and 128 target views, which we define as the wide-view baseline. For DL3DV, we evaluate 140 scenes, each with 16 context and 64 target views; whereas on ACID, we follow the wide-view baseline as in (2). For scene generation, we select 200 scenes, each with 192 target views, where we use the first frame as the conditioning and select 12 anchor poses equally spaced across 192 frames (c.f. Sec. 3.4).

**Evaluation Metrics.** We evaluate the novel-view synthesis and generation quality using Peak-Signal-to-Noise Ratio (PSNR), Perceptual Similarity (LPIPS) [68], Structural Similarity (SSIM), Frechet Video Distance (FVD) [49], and Frechet Inception Distance (FID) [14]. Moreover, for multi-view consistency, we use MET3R [1] and for transferability, we use the True-Pose-Similarity (TPS) metric proposed in concurrent work [33].

**Training Details.** We train SceneTok on 4 Nvidia A100 (40GB) GPU with an effective batch size of 128 with gradient checkpointing, for 760K iterations ( $\approx 11$  epochs), resulting in a total of roughly  $\approx 250$  (GPU+CPU) hours. Furthermore, we train SceneGen for 1M iterations, which takes  $\approx 238$  (GPU+CPU) hours at an effective batch size of 96 on 4 Nvidia A100 (80 GB). Please refer to Appendix Sec. A for more details.

### 4.2. Novel View Synthesis

In this section, we evaluate SceneTok on: (1) novel-view synthesis and (2) transferability of novel trajectories that de-



Figure 4. **Qualitative NVS.** (□, □, □) denote the context views (only four is shown), the target rendering of SceneTok and the ground-truth target view (only one is shown) respectively. While the baselines suffer from blur artifacts even without compression, SceneTok produces cleaner renderings and better details from a small set of scene tokens. More examples in Appendix Sec. D.

	DL3DV-140						Zero-Shot ACID					
	Repr. Size (#Floats)	PSNR ↑	LPIPS ↓	SSIM ↑	rFVD ↓	rFID ↓	Repr. Size (#Floats)	PSNR ↑	LPIPS ↓	SSIM ↑	rFVD ↓	rFID ↓
<i>Requires Target Views</i>												
RayZer [18]	2.36M	26.89	0.154	0.834	87.41	14.75	-	-	-	-	-	-
<i>Explicit Representation</i>												
MVSplat360 [10]	174.32M	18.54	0.278	0.629	314.28	21.95	74.71M	21.75	0.280	0.701	294.86	43.24
DepthSplat [56]	108.27M	21.86	0.192	0.769	423.91	20.90	46.40M	21.52	0.216	0.772	351.97	29.20
Long-LRM [73]	492.99M	23.06	0.181	0.796	519.19	26.56	-	-	-	-	-	-
<i>Latent Representation</i>												
LVSM [19]	1.57M	21.44	0.334	0.595	522.57	37.54	1.57M	23.67	0.296	0.663	269.63	34.99
<b>SceneTok</b>	<b>65.54K</b>	<b>21.95</b>	<b>0.219</b>	<b>0.660</b>	<b>246.51</b>	<b>19.12</b>	<b>32.77K</b>	<b>24.21</b>	<b>0.217</b>	<b>0.683</b>	<b>129.77</b>	<b>13.94</b>

Table 2. **Quantitative comparison of NVS quality on DL3DV-140 and ACID:** SceneTok achieves better performance in most metrics as compared to baselines with explicit and latent representations on DL3DV-140 and superior generalization on zero-shot ACID. Note that the models used in ACID were trained on RealEstate10K (c.f. Tab. 1).

	R. Acc. ↑			T. Acc. ↑			AUC ↑		
	10°	20°	30°	10°	20°	30°	10°	20°	30°
RayZer [18]	26.16	42.50	54.45	07.82	23.75	41.59	0.007	0.020	0.096
LVSM [19]	48.07	65.60	74.56	14.25	33.02	49.60	0.032	0.103	0.178
<b>SceneTok</b>	<b>75.81</b>	<b>86.47</b>	<b>89.86</b>	<b>62.44</b>	<b>80.31</b>	<b>86.48</b>	<b>0.307</b>	<b>0.492</b>	<b>0.593</b>

Table 3. **Transferability on scene pairs from DL3DV-140.** We compare the transferability of novel camera trajectories by swapping target poses of scene pairs and quantify using TPS [33].

	MEt3R <sub>RE10K</sub> ↓	MEt3R <sub>DL3DV</sub> ↓	MEt3R <sub>ACID</sub> ↓
MVSplat360 [10]	0.0220	0.0579	0.0196
LVSM [19]	0.0162	0.0541	<b>0.0126</b>
<b>SceneTok</b>	<b>0.0149</b>	<b>0.0538</b>	0.0133

Table 4. **Multi-View Consistency.** SceneTok achieves good pairwise consistency with MEt3R [1] across all dataset.

viate from the inputs. In (1), we compare existing works that we broadly categorize into *explicit* and *latent* representations. In (2), we only compare against the latter, as any classical 3D representation always performs true NVS.

**Reconstruction Quality.** In Tab. 1 and 2, we evaluate SceneTok and the baselines on RealEstate10K [72], DL3DV [23], and zero-shot performance on ACID [25]. We

observe an overall improvement over the baselines in most metrics across all NVS settings while significantly reducing the representation size in terms of the number of 32-bit floating point numbers. Although Long-LRM [73] achieves superior PSNR, LPIPS, and SSIM at the cost of a very large representation size, it falls short in rFVD and rFID. On the other hand, RayZer [18] surpasses all baselines, including ours, in all metrics. However, Rayzer requires the target views as input, thus, cannot render novel trajectories (c.f. [33] and Tab. 3). Also, there might be basic statistics leaking through the pose encoder. DepthSplat achieves superior SSIM due to the use of extensive depth supervision during training and inference, whereas our method is self-supervised and is trained end-to-end with the rectified flow loss. Compared to our method, LVSM [19] and RayZer use a dimensionality of  $3072 \times (512/768)$  respectively, which is significantly larger and ill-suited for generation with diffusion models. This is also true for all other 3D Gaussian-based baselines. We use a relatively light-weight video rectified flow model with 595M parameters, and we note that our decoder is efficient, attributed to the use of VideoD-

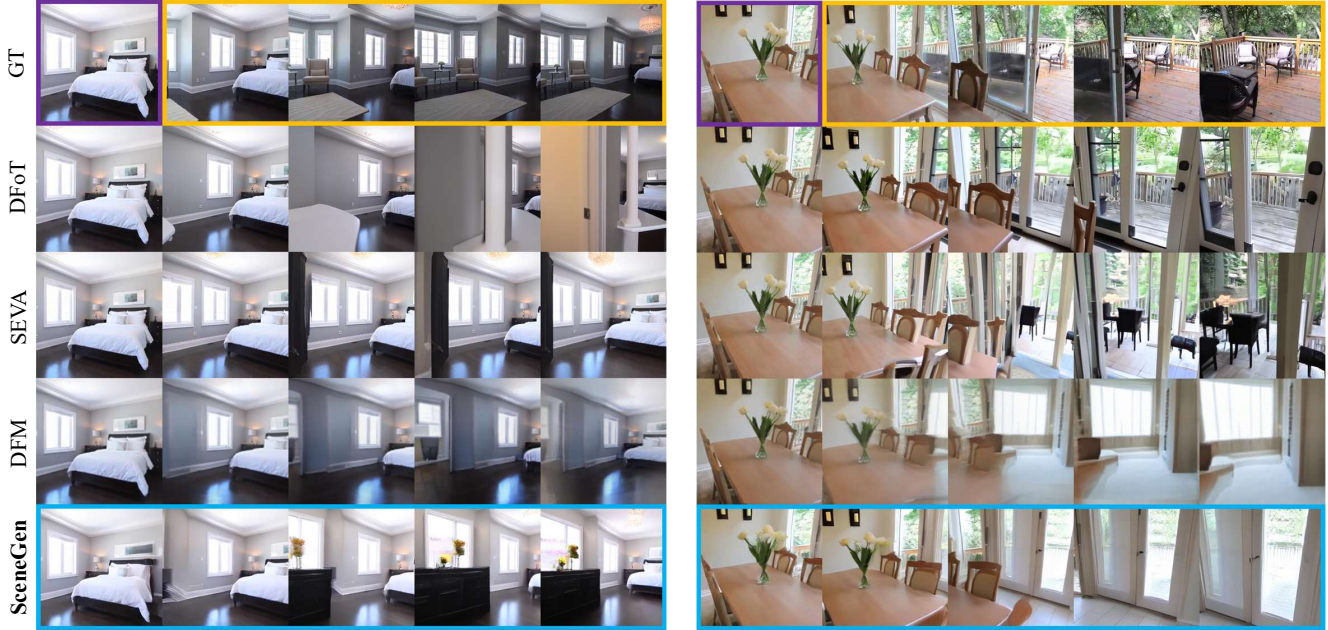


Figure 5. **Qualitative single-view generation comparison.** (□, □, □) represents the input view, the rendered target views from the generated scene, and the ground-truth views respectively. DFM produces blurry results and struggles to generate complete structures. Although our method falls short in generating high-quality, high-frequency details when compared to DFoT, which performs pixel-space diffusion, and the foundational generative model SEVA, it is significantly more efficient (c.f. Tab. 5). More examples in Appendix Sec. D.

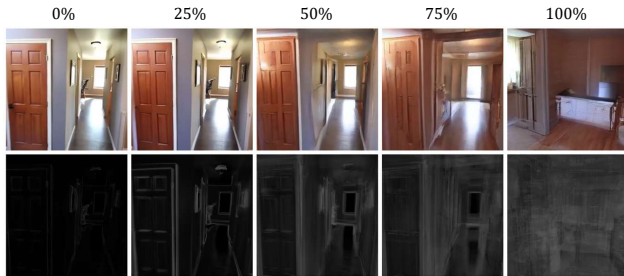


Figure 6. **RGB and per-pixel variance vs mask-ratio.** We show a single RGB rendering with its variance map (over 10 samples) on increasing mask-ratios of  $0 \rightarrow 100\%$ . Note that we scale the variance map by a factor of 1.5.

CAE [38] and our compressed token representation. This allows us to render 32 novel views at a time in 1 second with 25 sampling steps. In Fig. 4, we show qualitative comparisons of the rendered results on each dataset.

**Transferability on Novel Trajectories.** We further evaluate SceneTok on trajectories that deviate from the context trajectory in Tab. 3. We aim to verify that our method can generalize well to novel trajectories and perform true NVS [33] instead of view interpolation. We split DL3DV-140 [23] scenes into 70 pairs, where we predict the scene tokens from the context views of scene A and render the target trajectory of scene B, while measuring pose accuracy with TPS [33] across 3 error thresholds. We find that our model follows the given trajectories more faithfully, as indicated by higher TPS, and surpasses LVSM [19] and RayZer [18],

	PSNR $\uparrow$	LPIPS $\downarrow$	SSIM $\uparrow$	gFVD $\downarrow$	gFID $\downarrow$	Inference (s) $\downarrow$	MEI3R $\downarrow$
DFM [48]	<b>15.86</b>	0.468	<b>0.529</b>	566.71	52.64	630	0.0225
DFoT [44]	14.76	0.433	0.469	220.36	35.40	146	0.0194
SEVA [71]	14.41	0.442	0.450	<b>133.00</b>	<b>17.69</b>	1620	0.0164
<b>SceneGen</b>	15.12	<b>0.415</b>	0.493	157.89	18.90	<b>26 (11 + 16)</b>	<b>0.0156</b>

Table 5. **Single-View Generation Comparison.** We test SceneGen and the baselines on 200 scenes, each with 192 frames. SceneGen performs comparably to previous works in metrics but is significantly faster in generation ( $\approx 11s$ ).

which represent the state-of-the-art among generalizable 3D reconstruction methods without an explicit 3D representation. Please refer to Fig. 17, and 18 in the appendix for qualitative comparisons.

### 4.3. Scene Generation

We evaluate our latent scene generation model on the single-view generation task, and compare with DFM [48], DFoT [44], and SEVA [71], in terms of the FID and FVD, in addition to PSNR, LPIPS, and SSIM. Table 5 shows the quantitative results, and the qualitative results are provided in Fig. 5. The quantitative results suggest that SceneGen is on par with large-scale multi-view generation models. Qualitatively, we can observe that DFoT and SEVA still generate slightly better high-frequency details. DFoT generates in pixel space without perceptual compression; therefore, it can produce high-frequency structures well. SEVA, on the other hand, has superior FID and FVD, which we attribute to the use of a large-scale closed-source dataset for training. In contrast, our method, DFM, and DFoT

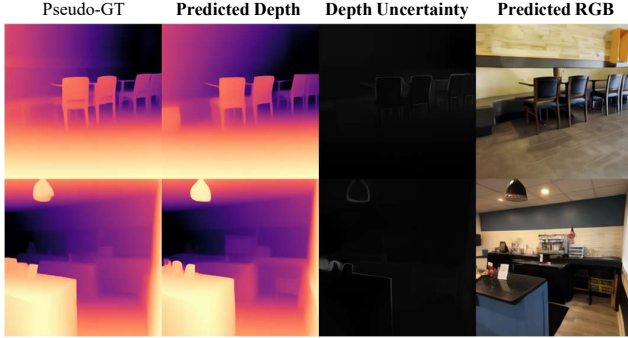


Figure 7. **Depth decoding on frozen SceneTok on DL3DV-140.** We show two scenes with the pseudo-GT from UniDepthV2 [39] and the predicted depth renderings with our finetuned depth decoder along with depth uncertainty and the RGB rendering. More examples are provided in Fig. 16 in the appendix.

are all trained exclusively on RealEstate10K. Moreover, we achieve significant improvements in inference speed, as shown in Tab. 5. The inference speed is recorded on Nvidia H100 (80GB) for all methods and for SceneGen we show the combined inference time for generating the scene tokens (11s) and rendering 192 target views (16s). Unlike DFM, SEVA, and DFoT, which ran into OOM issues, SceneGen can also run on a local Nvidia RTX 4090 (24GB), with an even lower total inference time of 10s (5s for generation and 5s for rendering 192 views).

#### 4.4. Analysis on Scene Tokens

We perform further analysis on the token representation to understand what information is encoded and how it is provided to the decoder. We do this in three ways: (1) freezing the token space and decoding depth maps, (2) masking elements of the representation by dropping tokens, and (3) masking observations by dropping context views. In all experiments, we compute a per-pixel variance map of the output depth/RGB renderings across different noise initializations to visualize uncertainty.

**Depth Decoding.** We use pre-trained SceneTok on DL3DV [23] and freeze the encoder. We replace the target images with depth maps predicted by UniDepthV2 [39] as pseudo ground-truth and compute video latents by duplicating the channels  $\times 3$ , and then fine-tune the pretrained decoder. In Fig 7, we show that SceneTok inherently encodes geometric cues without any explicit supervision and can render plausible depth maps with minimal uncertainty.

**Masking Scene Tokens.** We showcase the effect of randomly masking a percentage of the scene tokens, as shown in Fig. 6, which displays the RGB renderings and the corresponding per-pixel variance map for mask ratios of 0%, 25%, 50%, 75%, and 100% (where we effectively perform unconditional sampling). With 0% masked tokens, the overall structure of the scene is well-encoded in the tokens, as



Figure 8. **RGB and per-pixel variance vs context views.** (□, □, □) denote different target views and □ denotes the 12 context views. As we increase  $n$ , information in the tokens increases, and the variance reduces accordingly for the newly observed regions. Note that we scale the variance map by a factor of 2.

indicated by low overall variance. In this case, the generative decoder only samples minor, high-frequency details around edges. By masking more tokens, we effectively remove information from the scene; therefore, we observe an increase in output variance.

**Masking Context Views.** Alternatively, we drop the context views to visualize the effect more locally within the scene. Specifically, we keep the first  $n$  out of 12 context views and drop the rest; this way, we progressively add/remove sections from the representation. In Fig. 8, we show the corresponding RGB rendering and the variance map for  $n \in \{2, 6, 12\}$ . We observe that, with increasing  $n$ , the output variance progressively reduces, and regions covered by the tokens exhibit lower variance. This shows that our scene token plays a crucial role in providing most of the information to the decoder. We provide further quantitative analysis in Appendix Sec. C.

## 5. Conclusion

We introduced SceneTok, an autoencoder to encode scene information from view sets into an unstructured, highly compressed token space. The architecture consists of a scene perceiver module and a generative decoder. We demonstrated that the autoencoder reaches state-of-the-art reconstruction quality, is very efficient, and decodes from an order-of-magnitude stronger compression. We demonstrated that the latent space lends itself to efficient scene generation in 8 seconds on a single consumer GPU.

**Limitations and Future Work.** SceneTok introduces a novel concept for scene encoding but still has limitations, for example in reconstructing consistent high-frequency details. We see potential for improvements with better image compressors or through structured latent spaces, utilizing findings from recent works on image tokenization [2, 64].

## Acknowledgements

This project was partially funded by the Saarland/Intel Joint Program on the Future of Graphics and Media. Jan Eric Lenssen is supported by the German Research Foundation (DFG) - 556415750 (Emmy Noether Programme, project: Spatial Modeling and Reasoning).

## References

- [1] Mohammad Asim, Christopher Wewer, Thomas Wimmer, Bernt Schiele, and Jan Eric Lenssen. Met3r: Measuring multi-view consistency in generated images. In *CVPR*, 2024. 3, 5, 6
- [2] Roman Bachmann, Jesse Allardice, David Mizrahi, Enrico Fini, Oğuzhan Fatih Kar, Elmira Amirloo, Alaaeldin El-Nouby, Amir Zamir, and Afshin Dehghan. Flextok: Resampling images into 1d token sequences of flexible length. In *ICML*, 2025. 2, 8
- [3] Eric R. Chan, Koki Nagano, Matthew A. Chan, Alexander W. Bergman, Jeong Joon Park, Axel Levy, Miika Aittala, Shalini De Mello, Tero Karras, and Gordon Wetzstein. GeNVS: Generative novel view synthesis with 3D-aware diffusion models. In *arXiv*, 2023. 1
- [4] David Charatan, Sizhe Li, Andrea Tagliasacchi, and Vincent Sitzmann. pixelsplat: 3d gaussian splats from image pairs for scalable generalizable 3d reconstruction. In *CVPR*, 2024. 1, 2
- [5] Anpei Chen, Zexiang Xu, Fuqiang Zhao, Xiaoshuai Zhang, Fanbo Xiang, Jingyi Yu, and Hao Su. Mvsnerf: Fast generalizable radiance field reconstruction from multi-view stereo. In *Proceedings of the IEEE/CVF International Conference on Computer Vision*, pages 14124–14133, 2021. 2
- [6] Boyuan Chen, Diego Martí Monsó, Yilun Du, Max Simchowitz, Russ Tedrake, and Vincent Sitzmann. Diffusion forcing: next-token prediction meets full-sequence diffusion. In *Proceedings of the 38th International Conference on Neural Information Processing Systems*, Red Hook, NY, USA, 2024. Curran Associates Inc. 2
- [7] Boyuan Chen, Zhuo Xu, Sean Kirmani, Brain Ichter, Dorsa Sadigh, Leonidas Guibas, and Fei Xia. Spatialvlm: Endowing vision-language models with spatial reasoning capabilities. In *Proceedings of the IEEE/CVF Conference on Computer Vision and Pattern Recognition (CVPR)*, pages 14455–14465, 2024. 1
- [8] Junyu Chen, Han Cai, Junsong Chen, Enze Xie, Shang Yang, Haotian Tang, Muyang Li, Yao Lu, and Song Han. Deep compression autoencoder for efficient high-resolution diffusion models. In *ICLR*, 2025. 2
- [9] Yuedong Chen, Haofei Xu, Chuanxia Zheng, Bohan Zhuang, Marc Pollefeys, Andreas Geiger, Tat-Jen Cham, and Jianfei Cai. Mvsplat: Efficient 3d gaussian splatting from sparse multi-view images. In *NeurIPS*, 2024. 1, 2, 5
- [10] Yuedong Chen, Chuanxia Zheng, Haofei Xu, Bohan Zhuang, Andrea Vedaldi, Tat-Jen Cham, and Jianfei Cai. Mvsplat360: Feed-forward 360 scene synthesis from sparse views. In *NeurIPS*, 2024. 2, 5, 6
- [11] An-Chieh Cheng, Hongxu Yin, Yang Fu, Qiushan Guo, Ruihan Yang, Jan Kautz, Xiaolong Wang, and Sifei Liu. Spatialrgpt: Grounded spatial reasoning in vision-language models. In *NeurIPS*, 2024. 1
- [12] Patrick Esser, Robin Rombach, and Björn Ommer. Taming transformers for high-resolution image synthesis. In *CVPR*, 2021. 2
- [13] Ruiqi Gao, Aleksander Hoł yński, Philipp Henzler, Arthur Brussee, Ricardo Martin-Brualla, Pratul Srinivasan, Jonathan T. Barron, and Ben Poole. Cat3d: Create anything in 3d with multi-view diffusion models. In *NeurIPS*, 2024. 1, 2, 3
- [14] Martin Heusel, Hubert Ramsauer, Thomas Unterthiner, Bernhard Nessler, and Sepp Hochreiter. Gans trained by a two time-scale update rule converge to a local nash equilibrium. In *Proceedings of the 31st International Conference on Neural Information Processing Systems*, page 6629–6640, Red Hook, NY, USA, 2017. Curran Associates Inc. 5
- [15] Jonathan Ho and Tim Salimans. Classifier-free diffusion guidance. In *NeurIPS 2021 Workshop on Deep Generative Models and Downstream Applications*, 2021. 3
- [16] Jonathan Ho, Ajay Jain, and Pieter Abbeel. Denoising diffusion probabilistic models. In *NeurIPS*, 2020. 2
- [17] Siyuan Huang, Siyuan Qi, Yinxue Xiao, Yixin Zhu, Ying Nian Wu, and Song-Chun Zhu. Cooperative holistic scene understanding: Unifying 3d object, layout, and camera pose estimation. In *Advances in Neural Information Processing Systems*, pages 206–217, 2018. 1
- [18] Hanwen Jiang, Hao Tan, Peng Wang, Haian Jin, Yue Zhao, Sai Bi, Kai Zhang, Fujun Luan, Kalyan Sunkavalli, Qixing Huang, et al. Rayzer: A self-supervised large view synthesis model. In *ICCV*, 2025. 1, 2, 5, 6, 7
- [19] Haian Jin, Hanwen Jiang, Hao Tan, Kai Zhang, Sai Bi, Tianyuan Zhang, Fujun Luan, Noah Snavely, and Zexiang Xu. Lvsm: A large view synthesis model with minimal 3d inductive bias. In *ICLR*, 2025. 1, 2, 5, 6, 7
- [20] M. Johari, Y. Lepoittevin, and F. Fleuret. Geonerf: Generalizing nerf with geometry priors. In *Proceedings of the IEEE International Conference on Computer Vision and Pattern Recognition (CVPR)*, 2022. 2
- [21] Heewoo Jun and Alex Nichol. Shap-e: Generating conditional 3d implicit functions, 2023. 3
- [22] Bernhard Kerbl, Georgios Kopanas, Thomas Leimkühler, and George Drettakis. 3d gaussian splatting for real-time radiance field rendering. *ACM Transactions on Graphics*, 42(4), 2023. 1
- [23] Lu Ling, Yichen Sheng, Zhi Tu, Wentian Zhao, Cheng Xin, Kun Wan, Lantao Yu, Qianyu Guo, Zixun Yu, Yawen Lu, et al. D13dv-10k: A large-scale scene dataset for deep learning-based 3d vision. In *Proceedings of the IEEE/CVF Conference on Computer Vision and Pattern Recognition*, pages 22160–22169, 2024. 5, 6, 7, 8
- [24] Yaron Lipman, Ricky T. Q. Chen, Heli Ben-Hamu, Maximilian Nickel, and Matthew Le. Flow matching for generative modeling. In *The Eleventh International Conference on Learning Representations*, 2023. 4

- [25] Andrew Liu, Richard Tucker, Varun Jampani, Ameesh Makadia, Noah Snavely, and Angjoo Kanazawa. Infinite nature: Perpetual view generation of natural scenes from a single image. In *Proceedings of the IEEE/CVF International Conference on Computer Vision (ICCV)*, 2021. 5, 6
- [26] Ruoshi Liu, Rundi Wu, Basile Van Hoorick, Pavel Tokmakov, Sergey Zakharov, and Carl Vondrick. Zero-1-to-3: Zero-shot one image to 3d object, 2023. 3
- [27] Kingchao Liu, Chengyue Gong, and qiang liu. Flow straight and fast: Learning to generate and transfer data with rectified flow. In *The Eleventh International Conference on Learning Representations*, 2023. 4
- [28] Xiaoxiao Long, Yuan-Chen Guo, Cheng Lin, Yuan Liu, Zhiyang Dou, Lingjie Liu, Yuexin Ma, Song-Hai Zhang, Marc Habermann, Christian Theobalt, and Wenping Wang. Wonder3d: Single image to 3d using cross-domain diffusion. In *Proceedings of the IEEE/CVF Conference on Computer Vision and Pattern Recognition (CVPR)*, pages 9970–9980, 2024. 3
- [29] Wufei Ma, Yu-Cheng Chou, Qihao Liu, Xingrui Wang, Celso M de Melo, Jianwen Xie, and Alan Yuille. Spatialreasoner: Towards explicit and generalizable 3d spatial reasoning. In *Advances in Neural Information Processing Systems*, 2025. 1
- [30] Xindian Ma, Wenyuan Liu, Peng Zhang, and Nan Xu. 3d-rpe: Enhancing long-context modeling through 3d rotary position encoding. *AAAI*, 2025. 4
- [31] Leland McInnes, John Healy, Nathaniel Saul, and Lukas Grossberger. Umap: Uniform manifold approximation and projection. *The Journal of Open Source Software*, 2018. 4
- [32] Ben Mildenhall, Pratul P. Srinivasan, Matthew Tancik, Jonathan T. Barron, Ravi Ramamoorthi, and Ren Ng. Nerf: Representing scenes as neural radiance fields for view synthesis. In *ECCV*, 2020. 1
- [33] Thomas W Mitchel, Hyunwoo Ryu, and Vincent Sitzmann. True self-supervised novel view synthesis is transferable. In *arXiv preprint arXiv:2510.13063*, 2025. 1, 2, 5, 6, 7
- [34] Alex Nichol, Heewoo Jun, Prafulla Dhariwal, Pamela Mishkin, and Mark Chen. Point-e: A system for generating 3d point clouds from complex prompts, 2022. 3
- [35] Yinyu Nie, Xiaoguang Han, Shihui Guo, Yujian Zheng, Jian Chang, and Jian Jun Zhang. Total3dunderstanding: Joint layout, object pose and mesh reconstruction for indoor scenes from a single image. In *IEEE/CVF Conference on Computer Vision and Pattern Recognition (CVPR)*, 2020. 1
- [36] Niki Parmar, Ashish Vaswani, Jakob Uszkoreit, Lukasz Kaiser, Noam Shazeer, Alexander Ku, and Dustin Tran. Image transformer. In *ICML*, 2018. 2
- [37] William Peebles and Saining Xie. Scalable diffusion models with transformers. In *ICCV*, 2023. 3
- [38] Xiangyu Peng, Zangwei Zheng, Chenhui Shen, Tom Young, Xinying Guo, Binluo Wang, Hang Xu, Hongxin Liu, Mingyan Jiang, Wenjun Li, Yuhui Wang, Anbang Ye, Gang Ren, Qianran Ma, Wanying Liang, Xiang Lian, Xiwen Wu, Yuting Zhong, Zhuangyan Li, Chaoyu Gong, Guojun Lei, Leijun Cheng, Limin Zhang, Minghao Li, Ruijie Zhang, Silan Hu, Shijie Huang, Xiaokang Wang, Yuanheng Zhao, Yuqi Wang, Ziang Wei, and Yang You. Open-sora 2.0: Training a commercial-level video generation model in 200k. *arXiv preprint arXiv:2503.09642*, 2025. 2, 4, 7, 1, 3, 5
- [39] Luigi Piccinelli, Christos Sakaridis, Yung-Hsu Yang, Mattia Segu, Siyuan Li, Wim Abbeels, and Luc Van Gool. UniDepthV2: Universal monocular metric depth estimation made simpler, 2025. 8, 5
- [40] Barbara Roessle, Norman Müller, Lorenzo Porzi, Samuel Rota Bulò, Peter Kotschieder, Angela Dai, and Matthias Nießner. L3dg: Latent 3d gaussian diffusion. In *SIGGRAPH Asia 2024 Conference Papers*, 2024. 3
- [41] Robin Rombach, Andreas Blattmann, Dominik Lorenz, Patrick Esser, and Björn Ommer. High-resolution image synthesis with latent diffusion models. In *CVPR*, 2022. 2
- [42] Mehdi S. M. Sajjadi, Aravindh Mahendran, Thomas Kipf, Etienne Pot, Daniel Duckworth, Mario Lucic, and Klaus Greff. Rust: Latent neural scene representations from unposed imagery. In *CVPR*, 2024. 2
- [43] Vincent Sitzmann, Michael Zollhöfer, and Gordon Wetzstein. Scene representation networks: Continuous 3d-structure-aware neural scene representations. In *NeurIPS*, 2019. 2
- [44] Kiwhan Song, Boyuan Chen, Max Simchowitz, Yilun Du, Russ Tedrake, and Vincent Sitzmann. History-guided video diffusion. In *ICML*, 2025. 1, 2, 3, 4, 5, 7
- [45] Jianlin Su, Murtadha Ahmed, Yu Lu, Shengfeng Pan, Wen Bo, and Yunfeng Liu. Roformer: Enhanced transformer with rotary position embedding. *Neurocomput.*, 568(C), 2024. 4
- [46] Stanislaw Szymonowicz, Jason Y. Zhang, Pratul Srinivasan, Ruiqi Gao, Arthur Brussee, Aleksander Holynski, Ricardo Martin-Brualla, Jonathan T. Barron, and Philipp Henzler. Bolt3d: Generating 3d scenes in seconds. In *ICCV*, 2025. 1, 2
- [47] Jiayang Tang, Jiawei Ren, Hang Zhou, Ziwei Liu, and Gang Zeng. Dreamgaussian: Generative gaussian splatting for efficient 3d content creation. In *ICLR*, 2024. 1
- [48] Ayush Tewari, Tianwei Yin, George Cazenavette, Semon Rezchikov, Joshua B. Tenenbaum, Frédo Durand, William T. Freeman, and Vincent Sitzmann. Diffusion with forward models: Solving stochastic inverse problems without direct supervision. In *NeurIPS*, 2023. 1, 3, 5, 7
- [49] Thomas Unterthiner, Sjoerd van Steenkiste, Karol Kurach, Raphaël Marinier, Marcin Michalski, and Sylvain Gelly. FVD: A new metric for video generation, 2019. 5
- [50] Team Wan, Ang Wang, Baole Ai, Bin Wen, Chaojie Mao, Chen-Wei Xie, Di Chen, Feiwu Yu, Haiming Zhao, Jianxiao Yang, Jianyuan Zeng, Jiayu Wang, Jingfeng Zhang, Jingen Zhou, Jinkai Wang, Jixuan Chen, Kai Zhu, Kang Zhao, Keyu Yan, Lianghua Huang, Mengyang Feng, Ningyi Zhang, Pandeng Li, Pingyu Wu, Ruihang Chu, Ruili Feng, Shiwei Zhang, Siyang Sun, Tao Fang, Tianxing Wang, Tianyi Gui, Tingyu Weng, Tong Shen, Wei Lin, Wei Wang, Wei Wang, Wenmeng Zhou, Wenten Wang, Wenting Shen, Wenyuan Yu, Xianzhong Shi, Xiaoming Huang, Xin Xu, Yan Kou, Yangyu Lv, Yifei Li, Yijing Liu, Yiming Wang, Yingya Zhang, Yitong Huang, Yong Li, You Wu, Yu Liu, Yulin Pan, Yun Zheng, Yuntao Hong, Yupeng Shi, Yutong Feng, Zeyinzi

- Jiang, Zhen Han, Zhi-Fan Wu, and Ziyu Liu. Wan: Open and advanced large-scale video generative models. *arXiv preprint arXiv:2503.20314*, 2025. 1, 2, 3, 5, 12, 13, 14, 15, 16, 17
- [51] Hanyu Wang, Saksham Suri, Yixuan Ren, Hao Chen, and Abhinav Shrivastava. LARP: Tokenizing videos with a learned autoregressive generative prior. In *ICLR*, 2025. 2
- [52] Qianqian Wang, Zhicheng Wang, Kyle Genova, Pratul Srinivasan, Howard Zhou, Jonathan T. Barron, Ricardo Martin-Brualla, Noah Snavely, and Thomas Funkhouser. Ibrnet: Learning multi-view image-based rendering. In *CVPR*, 2021. 2
- [53] Xin Wen, Bingchen Zhao, Ismail Elezi, Jiankang Deng, and Xiaojuan Qi. “Principal components” enable a new language of images. In *ICCV*, 2025. 2
- [54] Christopher Wewer, Kevin Raj, Eddy Ilg, Bernt Schiele, and Jan Eric Lenssen. latentsplat: Autoencoding variational gaussians for fast generalizable 3d reconstruction. In *ECCV*, 2024. 1, 2
- [55] Christopher Wewer, Bartłomiej Pogodzinski, Bernt Schiele, and Jan Eric Lenssen. Spatial reasoning with denoising models. In *International Conference on Machine Learning (ICML)*, 2025. 1
- [56] Haofei Xu, Songyou Peng, Fangjinhua Wang, Hermann Blum, Daniel Barath, Andreas Geiger, and Marc Pollefeys. Depthsplat: Connecting gaussian splatting and depth. In *CVPR*, 2025. 2, 5, 6
- [57] Zhuoyi Yang, Jiayan Teng, Wendi Zheng, Ming Ding, Shiyu Huang, Jiazheng Xu, Yuanming Yang, Wenyi Hong, Xiaohan Zhang, Guanyu Feng, Da Yin, Yuxuan Zhang, Weihang Wang, Yean Cheng, Bin Xu, Xiaotao Gu, Yuxiao Dong, and Jie Tang. Cogvideox: Text-to-video diffusion models with an expert transformer. In *ICLR*, 2025. 2
- [58] Jingfeng Yao, Cheng Wang, Wenyu Liu, and Xinggang Wang. Fasterdit: Towards faster diffusion transformers training without architecture modification. In *NeurIPS*, 2024. 4, 1, 2
- [59] Jingfeng Yao, Bin Yang, and Xinggang Wang. Reconstruction vs. generation: Taming optimization dilemma in latent diffusion models. In *CVPR*, 2025. 2, 3, 4
- [60] Taoran Yi, Jiemin Fang, Junjie Wang, Guanjun Wu, Lingxi Xie, Xiaopeng Zhang, Wenyu Liu, Qi Tian, and Xinggang Wang. Gaussiandreamer: Fast generation from text to 3d gaussians by bridging 2d and 3d diffusion models. In *CVPR*, 2024. 1
- [61] Alex Yu, Vickie Ye, Matthew Tancik, and Angjoo Kanazawa. pixelNeRF: Neural radiance fields from one or few images. In *CVPR*, 2021. 2
- [62] Alex Yu, Vickie Ye, Matthew Tancik, and Angjoo Kanazawa. pixelNeRF: Neural radiance fields from one or few images. In *CVPR*, 2021. 1
- [63] Qihang Yu, Mark Weber, Xueqing Deng, Xiaohui Shen, Daniel Cremers, and Liang-Chieh Chen. An image is worth 32 tokens for reconstruction and generation. In *NeurIPS*, 2024. 2
- [64] Sihyun Yu, Sangkyung Kwak, Huiwon Jang, Jongheon Jeong, Jonathan Huang, Jinwoo Shin, and Saining Xie. Representation alignment for generation: Training diffusion transformers is easier than you think. In *International Conference on Learning Representations*, 2025. 8
- [65] Wangbo Yu, Jinbo Xing, Li Yuan, Wenbo Hu, Xiaoyu Li, Zhipeng Huang, Xiangjun Gao, Tien-Tsin Wong, Ying Shan, and Yonghong Tian. Viewcrafter: Taming video diffusion models for high-fidelity novel view synthesis. *arXiv preprint arXiv:2409.02048*, 2024. 1, 2, 3
- [66] Cheng Zhang, Zhaopeng Cui, Yinda Zhang, Bing Zeng, Marc Pollefeys, and Shuaicheng Liu. Holistic 3d scene understanding from a single image with implicit representation. In *Proceedings of the IEEE/CVF Conference on Computer Vision and Pattern Recognition (CVPR)*, pages 8833–8842, 2021. 1
- [67] Kai Zhang, Sai Bi, Hao Tan, Yuanbo Xiangli, Nanxuan Zhao, Kalyan Sunkavalli, and Zexiang Xu. Gs-lrm: Large reconstruction model for 3d gaussian splatting. In *ECCV*, 2024. 1, 2
- [68] Richard Zhang, Phillip Isola, Alexei A Efros, Eli Shechtman, and Oliver Wang. The unreasonable effectiveness of deep features as a perceptual metric. In *CVPR*, 2018. 5
- [69] Sijie Zhao, Yong Zhang, Xiaodong Cun, Shaoshu Yang, Muyao Niu, Xiaoyu Li, Wenbo Hu, and Ying Shan. CV-VAE: A compatible video VAE for latent generative video models. In *NeurIPS*, 2024. 2
- [70] Yuyang Zhao, Chung-Ching Lin, Kevin Lin, Zhiwen Yan, Linjie Li, Zhengyuan Yang, Jianfeng Wang, Gim Hee Lee, and Lijuan Wang. Genxd: Generating any 3d and 4d scenes. In *ICLR*, 2025. 1
- [71] Jensen (Jinghao) Zhou, Hang Gao, Vikram Voleti, Aaryaman Vasishtha, Chun-Han Yao, Mark Boss, Philip Torr, Christian Rupprecht, and Varun Jampani. Stable virtual camera: Generative view synthesis with diffusion models. In *ICCV*, 2025. 1, 2, 3, 5, 7
- [72] Tinghui Zhou, Richard Tucker, John Flynn, Graham Fyffe, and Noah Snavely. Stereo magnification: Learning view synthesis using multiplane images. In *SIGGRAPH*, 2018. 5, 6
- [73] Chen Ziwen, Hao Tan, Kai Zhang, Sai Bi, Fujun Luan, Yicong Hong, Li Fuxin, and Zexiang Xu. Long-lrm: Long-sequence large reconstruction model for wide-coverage gaussian splats. In *ICCV*, 2025. 1, 2, 5, 6

# SceneTok: A Compressed, Diffusable Token Space for 3D Scenes

## Supplementary Material

The supplementary materials are structured as follows. First, we provide detailed information about our training procedure and the architecture for both SceneTok and SceneGen in Sec. A, ablation on the design choices for both models in Sec. B, a discussion on the choice of positional encoding, visualization of the latent space and further analysis into the uncertainty caused by adding or removing information from the scene tokens in Sec. C, and additional qualitative results for transferability on novel trajectories, novel-view synthesis, and single-view generation in Sec. D.

### A. Training and Architectural Details

#### A.1. SceneTok.

In Tab. 6, details of the model and training hyper-parameters, including the input and sampling configuration, are provided. In addition, Fig. 9 shows a single decoder block, where we first perform self-attention between latent (noisy) video tokens of the target views, followed by cross-attention to the scene tokens  $\mathcal{Z}$ .

**Choice of Input Coordinate System.** When encoding 3D scenes from view sets, we choose one input view as reference and ensure that all other view poses are given as relative pose w.r.t. to the chosen reference pose. The choice of reference frame can vary and can be augmented during training. The procedure ensures that the scene origin is always present in the input and that the scene is structured around this origin, improving model generalization. Anchoring the representation around the origin is also relevant for scene generation, as further discussed in Sec. 3.4.

**Camera-Controlled Video Rendering.** We use VideoD-CAE [38] (later also add WanVAE [50] c.f. Sec. B) as the tokenizer for the target views which allows for 32x spatial and 4x temporal compression. We assume each latent video frame is temporally localized and encodes four consecutive RGB frames. Therefore, we concatenate the corresponding ray maps along the channel dimension for these four frames. The high spatio-temporal compression allows us to render more frames quickly and efficiently.

**Data Augmentation.** During training, we randomly choose our reference frame from the  $N$  context views and compute the corresponding relative camera poses for the remaining context and target views. We also randomly flip images and their trajectories, as done in PixelSplat [4].

**Training Instability.** We observe some training instability (gradient spikes) during our training. We attribute this primarily to the use of mixed-precision, and it mainly occurs during the encoding stage. To assist with the training,

<i>Model Configurations</i>	Encoder	Decoder
Overall size	242M	595M
Hidden dimensions $d_H$	768	1024
Depth $L$	12	24
Number of heads	12	16
MLP ratio	4.0	4.0
2D RoPE	✓	✗
3D RoPE	✗	✓
Norm type	RMSNorm	RMSNorm
Camera conditioning	AdaLN	AdaLN
QK Norm	✗	✓
Activation	SwiGLU	SwiGLU
<i>Inputs Configurations</i>		
Raw shape	$N \times 256 \times 256 \times 3$	$M \times 256 \times 256 \times 3$
Temporal compression	$\times 1$	$\times 4$
Spatial compression	$\times 16$	$\times 32$
Token dimensions	32	128
Patch size	2	1
<i>Training Configurations</i>		
	RealEstate10K	DL3DV
Optimizer	AdamW	AdamW
Initial LR	$1.0e^{-4}$	$1.0e^{-4}$
LR decay steps	[20K, 150K, 500K]	[4K, 8K, 100K]
LR decay factor	0.4	0.4
Warmup steps	2000	2000
Gradient clip	0.01	0.01
Precision	bfloat16 (mixed)	bfloat16 (mixed)
Effective Batch size	128	64
Training steps	760K	1M
Freeze encoder after	150K	None
<i>Token Dimensionality</i>		
RealEstate10K / ACID	512 $\times$ 64	
DL3DV	1024 $\times$ 64	
<i>Sampling (Inference)</i>		
Steps	25	
CFG scale	1.0	

Table 6. **Summary of SceneTok.** We show the model, input, training and sampling our scene autoencoder. Both the encoder and the decoder using the transformer modules from LightningDiT [58] with additional modifications (c.f. Fig. 3 and Sec. 3).

we use a relatively lower gradient clipping value, skip the optimizer step when large gradient norms are detected, following [18, 19], later freeze the encoder, and continue fine-tuning the decoder on the frozen latent space.

#### A.2. SceneGen

During training, we use the encoder from SceneTok to predict the scene tokens  $\mathcal{Z}$  from the given context views  $\mathcal{X}_C$ . We then add noise to the scene tokens and denoise them with SceneGen. Fig. 9 shows the decoder block of SceneTok, which we reuse in SceneGen by replacing the keys and values, i.e.,  $\mathcal{Z}$  with  $[\mathcal{F}_I, \mathcal{A}]$ , which is a con-

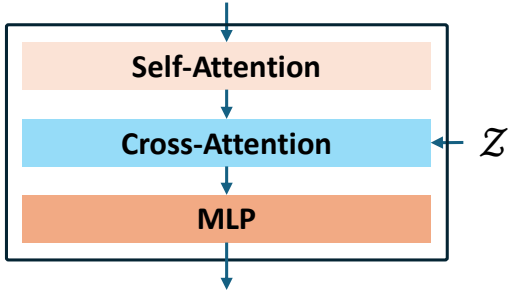


Figure 9. Decoder block of SceneTok.

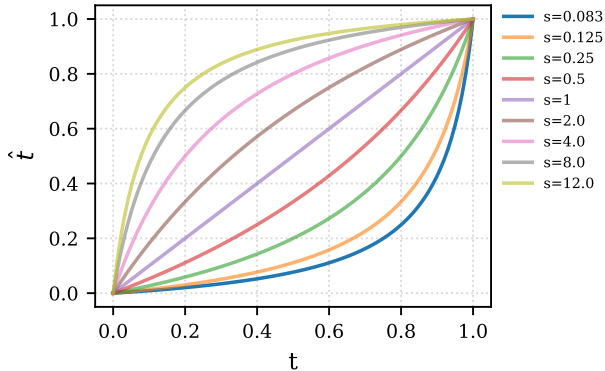


Figure 10. **Noise-level shift.** We plot the resulting timestep  $\hat{t}$  for different amount of  $s$ . For  $s > 1$ , we shift more towards higher noise and vice versa.

catenation of the input image tokens (from VA-VAE [59]) and the anchor tokens along the sequence dimension. The scene tokens serve as the inputs and outputs of our latent generation model.

In Tab. 7, details of the model and training hyperparameters, including the input and sampling configuration, are provided. Note that we use a higher timestep shift, which we found to improve the generation results. Specifically, we shift our timestep  $t \rightarrow \hat{t}$  as follows:

$$\hat{t} = \frac{st}{1 + (s-1)t}, \quad (6)$$

where  $s$  is the shift amount ( $\uparrow$  higher and  $\downarrow$  lower noise-levels). Refer to Sec. B for further quantitative ablation over different shifts. In Fig 10, we show the resulting shifted timestep  $\hat{t}$  for  $s > 1$  and  $s < 1$ .

**Data Augmentation.** During training, we augment our scene origin by randomly selecting a single context view as the reference. The corresponding anchors and conditioning camera are set relative to the reference frame (before predicting the scene tokens). The reference view is also used as the first input conditioning for the model. We also randomly flip the images and poses horizontally, similar to SceneTok.

<i>Model Configurations</i>	
Overall size	1.3B
Hidden dimensions $d_H$	1536
Depth $L$	24
Number of heads	24
MLP ratio	4.0
Norm type	RMSNorm
Camera conditioning	AdaLN
Anchor conditioning	CrossAtten
QK Norm	✓
Activation	SwiGLU
<i>Inputs Configurations</i>	
Raw shape	$512 \times 64$
Token dimensions	64
<i>Training Configurations</i>	
Optimizer	AdamW
Initial LR	$1.0e^{-4}$
LR decay steps	[100K, 250K, 400K]
LR decay factor	0.4
Warmup steps	2000
Gradient clip	0.1
Precision	bfloat16 (mixed)
Effective Batch size	96
Timestep weighting	Shifted Timestep
Timestep shift	12
Training steps	1M
<i>Sampling (Inference)</i>	
Steps	150
CFG scale	3.0
Timestep shift	12

Table 7. **Summary of SceneGen.** We show the model, input, training and sampling configurations for both versions of latent scene generation model. We use the transformer module from LightningDiT [58] with an additional cross attention module for input conditioning (c.f. Sec. 3.4).

## B. Ablation Studies

In this section, we provide further results where we ablate specific design choices of our method, including both SceneTok and SceneGen.

**Pretrained Video VAEs in SceneTok** We ablate the choice of the pre-trained image latent space (VideoD-CAE [38] in the main paper) by additionally evaluating WanVAE [50] as replacement for VideoDCAE. We found

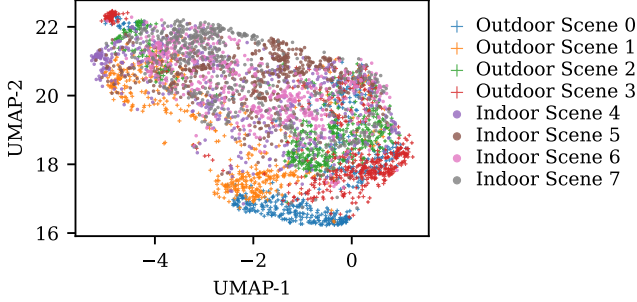


Figure 11. **UMAP plot of scene tokens across 8 scenes from RealEstate10K.** We compute the UMAP across all 512 tokens for 8 different scenes out of which 4 are outdoor (+) and indoor (•) scenes (c.f. Fig 12). We see that the majority of the tokens that belongs to the outdoor scenes are grouped closely together as compared to tokens from indoor scenes. This shows that our latent token space is discriminative in nature which is helpful for downstream generation task [59].

	Compression (Spatial, Temp.)	PSNR $\uparrow$	LPIPS $\downarrow$	SSIM $\uparrow$	rFVD $\downarrow$	rFID $\downarrow$
VideoDCAE [38]	$\times 32, \times 4$	<b>21.95</b>	<b>0.219</b>	<b>0.660</b>	246.51	19.12
WanVAE [50]	$\times 16, (\times 4 + 1)$	19.81	0.254	0.561	<b>189.74</b>	<b>14.30</b>

Table 8. **Ablation on pretrained Video VAEs in SceneTok decoder.** We achieve better high frequency details with the SceneTok renderer trained with WanVAE [50]. This partly due to smaller spatial compression as compared to VideoDCAE. From this, we conclude that SceneTok performance is bounded by the performance of the video VAEs and therefore, exploring better alternatives can potentially improve SceneTok.

that WanVAE achieves better high frequency details, which we attribute to its relatively lower spatial compression, i.e.,  $\times 16$ , as compared to  $\times 32$  in VideoDCAE and is indicated by superior rFID and rFVD in Tab. 8. However, it achieves slightly worse results in reconstruction metrics, which are sensitive to blur and camera inaccuracies. Refer to the qualitative examples in Sec. D where we provide results for both versions of SceneTok.

**Classifier-Free Guidance in SceneTok** We notice that even though we train our decoder both conditionally and unconditionally to allow classifier-free guidance [15] during NVS, we found that using a higher guidance scale reduces the quality, as shown in Tab. 9, causing over-saturated RGB renderings and, therefore, worse reconstruction metrics. From these insights, we later remove classifier-free guidance when training SceneTok on DL3DV and instead train it purely conditionally.

**Number of Tokens vs PSNR in SceneTok.** In Fig. 14, we show the performance of our model trained on an increasing number of scene tokens and observe that with more tokens, we achieve better reconstruction quality; however, we chose  $K = 1024$ , and increasing it further leads to early overfitting, and the quality saturates. We believe that our

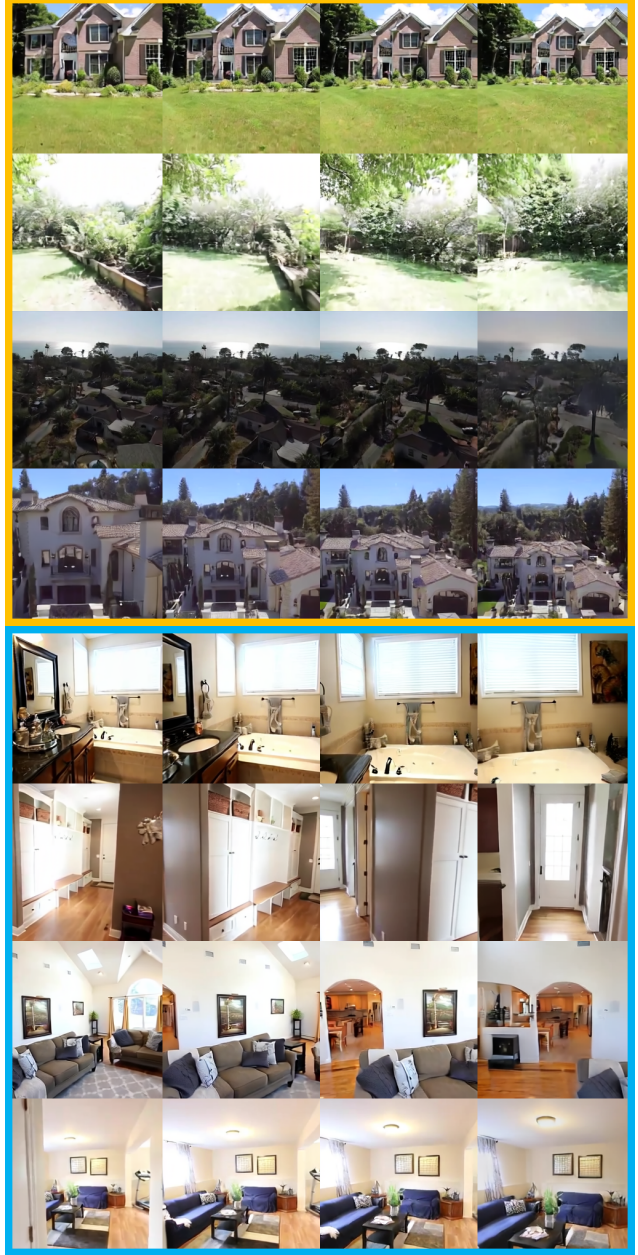


Figure 12. **Examples of outdoor and indoor scenes.** (□, □) denote outdoor and indoor scenes respectively. We show the RGB renderings of the scenes used in Fig. 11. Note that the scenes are ordered from top-to-bottom with indices  $0 \rightarrow 7$ .

method becomes upper bounded by the reconstruction quality of the pretrained video VAEs.

**Timestep Shift in SceneGen** We train the generative model with varying timestep shifts  $s \in 1.0, 4.0, 12.0$ . Overall, we found that shifting the noise-levels towards higher noise improves the results in terms of gFID in Fig. 10, suggesting that global structures emerge early on; therefore, it requires more steps to ensure better generation quality.



Figure 13. **Comparison of 3D vs 2D RoPE in the encoder.**  $\square$  denotes the input context views,  $(\square, \square)$  denotes the rendered targets with 3D RoPE [30] and 2D RoPE [45] respectively. We show 12 target views (RGB and variance map) from left-to-right where the first 6 columns shows the rendered views for the forward trajectory which aligns with the input order of the context and the remaining 6 views shows the backward trajectory. We observe higher variance for the backward trajectory for 3D RoPE and this indicates temporal bias of the scene tokens  $\mathcal{Z}$ . Note that we scale our variance map by a factor of 2.

Guidance Scale	PSNR $\uparrow$	LPIPS $\downarrow$	SSIM $\uparrow$	rFVD $\downarrow$	rFID $\downarrow$
1.0	24.22	0.157	0.784	68.39	9.13
2.0	24.35	0.151	0.792	69.52	9.69
3.0	24.05	0.158	0.787	79.60	11.25
4.0	23.71	0.166	0.778	89.11	12.75
5.0	23.49	0.174	0.771	101.24	14.19
6.0	23.28	0.183	0.764	112.04	16.00
7.0	23.06	0.190	0.757	124.79	17.375

Table 9. **Ablation on CFG scales in SceneTok.** We show the quantitative results for increasing guidance scale when rendering novel views. The experiment is performed on the wide-view baseline (c.f. Sec. 4.1) using 12 context views and 128 target views. We clearly see that using a smaller guidance scale performs better.

### C. Analysis on Scene Tokens

**Visualization of scene tokens.** In Fig. 11, we show the UMAP [31] plot of the scene tokens across 4 outdoor and 4 indoor scenes (refer to Fig 12). The goal is to understand the structure of the latent space in terms of its discriminativeness; i.e., tokens that belong to similar scenes (outdoor) should be clustered closely together, and vice versa. From the figure, we observe that the majority of the tokens belonging to outdoor scenes are grouped more compactly, and the inter group distance (especially between outdoor and indoor scene tokens) is large; i.e., we observe a clear separation between them.

**Temporal biases in the scene tokens.** We experimented with 2 choices of positional encoding for the input context

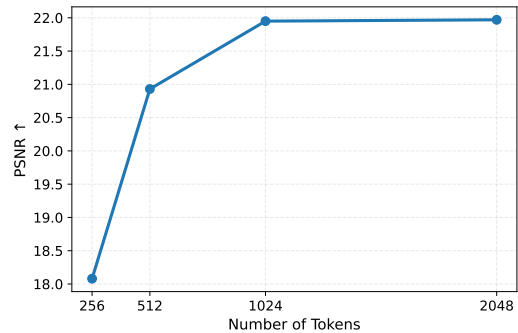


Figure 14. **PSNR vs Number of Tokens on DL3DV.** We train four variant of our method on different number of tokens while keeping the channel dimensions fixed.

Timestep Shift (s)	gFID $\downarrow$
1.0	19.99
4.0	19.04
12.0	18.90

Table 10. **Ablation on Timestep Shift in SceneGen.** We show the gFID three different timestep shifts where we train a separate model for each shift amount and also apply it during inference. We found that shifting towards higher noise results in better global structures as more steps are allocated in the low frequency regime.

view tokens: 1) 3D RoPE [30] and 2) 2D RoPE [45]. In the former, we assume a temporally ordered sequence of context view tokens  $\mathcal{X}_C = (\mathbf{x}_i \in \mathbb{R}^d)_{i=1}^N$  for each spatial location  $(i, j)$ . We perform a cycle consistency test, during which we render the target trajectory in both forward

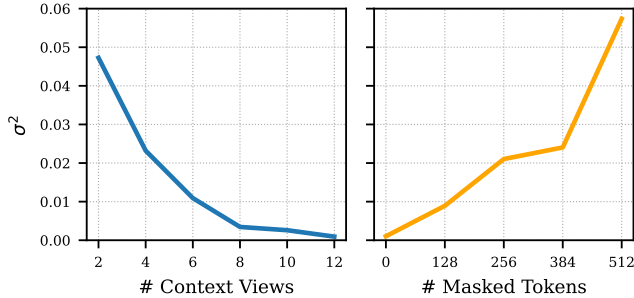


Figure 15. **Average per-pixel variance.** We plot the per-pixel variance averaged across the spatial and temporal dimension against increasing number of context views and masked tokens (out of 512 tokens). We show the plot for a single example scene.

and backward order. In Fig. 13, we show RGB renderings and the corresponding per-pixel variance maps for the forward and backward trajectory, where we can see that with 3D RoPE, we observe higher variance and poor renderings in the backward trajectory. The corresponding RGB renderings for the backward trajectory fail to follow the given camera poses correctly. In contrast, with 2D RoPE, we achieve significantly better cycle consistency, indicating invariance to the input order.

**Quantitative analysis of uncertainty.** In Fig. 15, we compute the per-pixel variance across 10 samples and average across the spatial and temporal dimensions. We observe a clear decreasing trend when we add more information to the scene tokens by progressively including more contextual views. Likewise, we observe a clear increasing trend when we remove information by masking the scene tokens.

## D. Additional Qualitative Results

**Transferability on scene pairs.** In Fig. 17 and 18, we provide qualitative visualizations of the transferability of novel trajectories that belong to a different scene. Specifically, consider the scene  $A$  (source) and  $B$  (transfer), we predict the scene tokens  $\mathcal{Z}$  from the context views of scene  $A$ , and render the trajectory from scene  $B$ . We show that, with our method, we can perform novel view rendering. In our experiments, we ensure that the center camera position and orientation of both trajectories from scene  $A$  and  $B$  are aligned at the same origin with respect to the first camera pose.

**Novel-view synthesis.** We show qualitative examples for NVS in Fig. 19, 20, 21, 22, 23, 24, 25, 26, 27 and 28 on RealEstate10K [72] and DL3DV [23], and observe that SceneTok (both trained on VideoDCAE [38] and WanVAE [50]) achieves better high-frequency details, as indicated by the faithful reconstruction of the text within the image (visible in the first example), and is well represented by our method even under high compression. Overall, we ob-

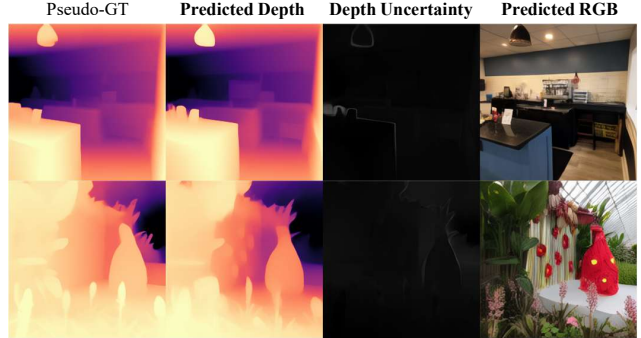


Figure 16. **Depth decoding on frozen SceneTok on DL3DV-140.** We show two scenes with the pseudo-GT from UniDepthV2 [39] and the predicted depth renderings with our finetuned depth decoder along with depth uncertainty and the RGB rendering.

serve better and cleaner renderings for our method in comparison to the existing works.

**Single-view generation.** We provide additional qualitative results for single-view generation in Fig. 29, and 30. Overall, we observe comparable generation quality, and our method is able to produce complete structures and geometry with partial observations. In comparison to DFoT [44] and SEVA [71], our method falls short of generating high-frequency details.

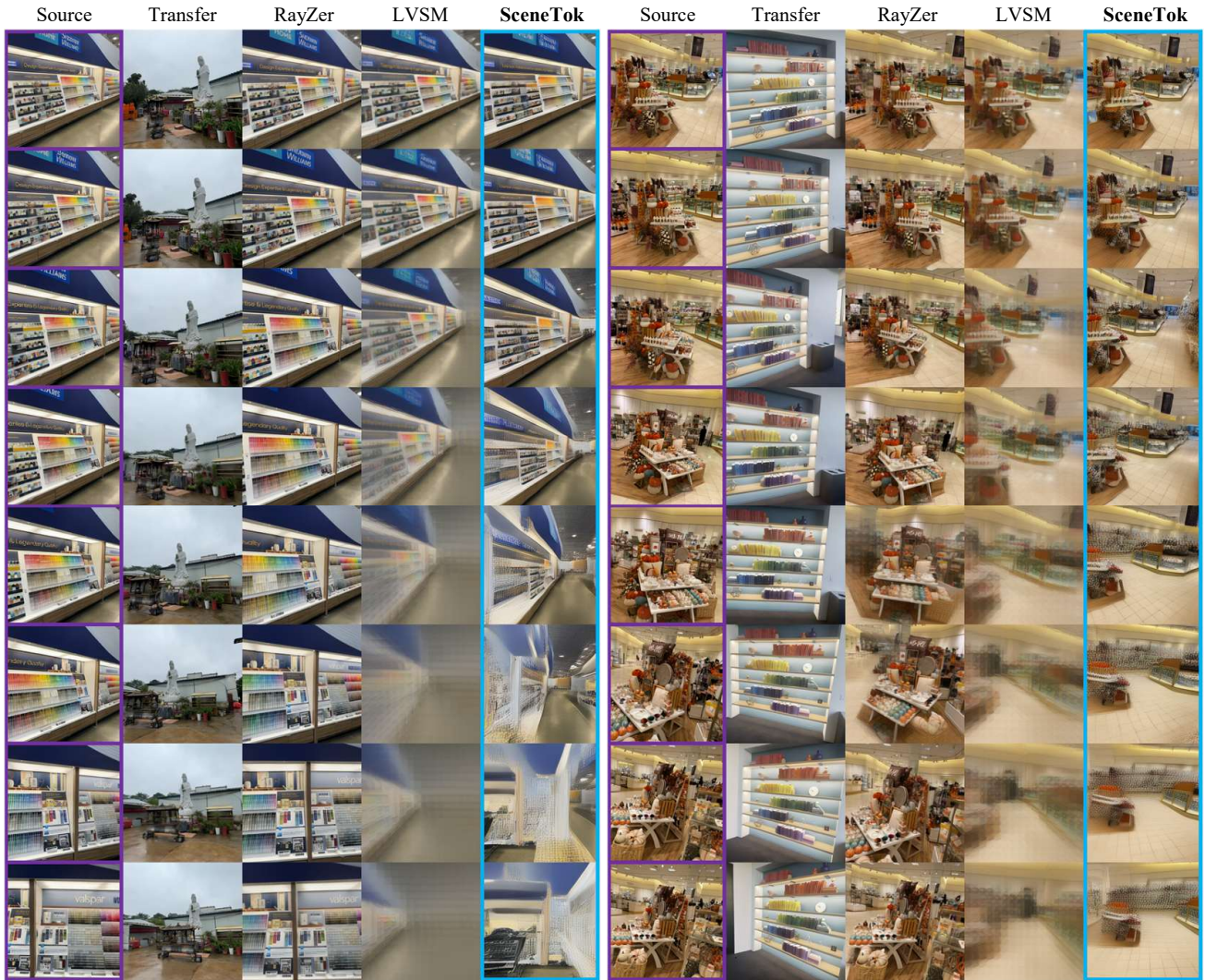


Figure 17. **Qualitative NVS on Transfer Trajectories.** (□, □) denotes the context views of the *source* scene, and the renderings of the *source* scene with trajectory from the *transfer* scene with `SceneTok`. Note that we can expect artifacts in regions that are not present in the context views and both `SceneTok`, and `LVSM` [19] are not trained for extrapolation. `RayZer` on the other hand fails to follow the given trajectory and only renders the original trajectory of the *source* scene.

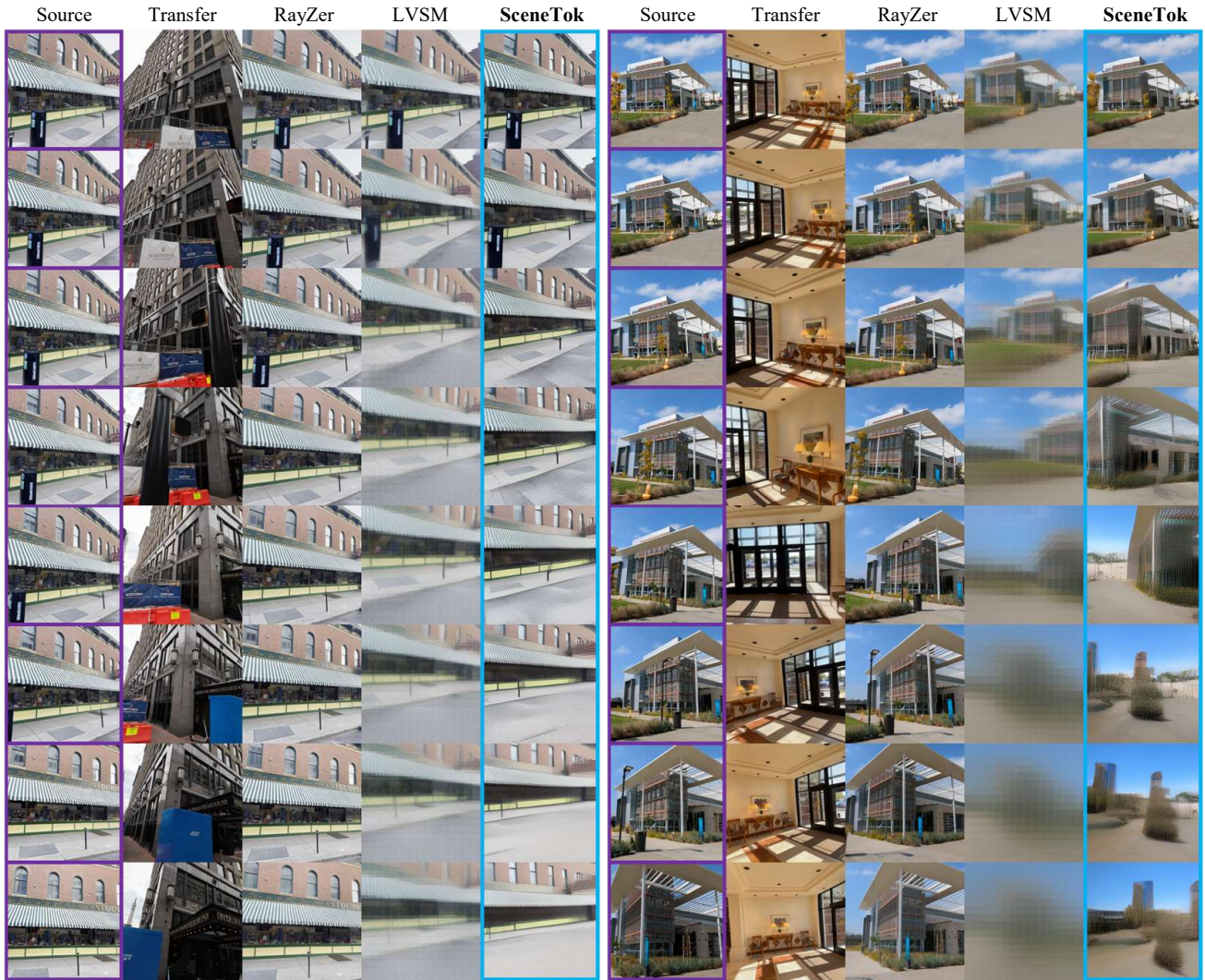


Figure 18. **Qualitative NVS on Transfer Trajectories.** (□, □) denotes the context views of the *source* scene, and the renderings of the *source* scene with trajectory from the *transfer* scene with SceneTok. Note that we can expect artifacts in regions that are not present in the context views and both SceneTok, and LVSM [19] are not trained for extrapolation. RayZer on the other hand fails to follow the given trajectory and only renders the original trajectory of the *source* scene.

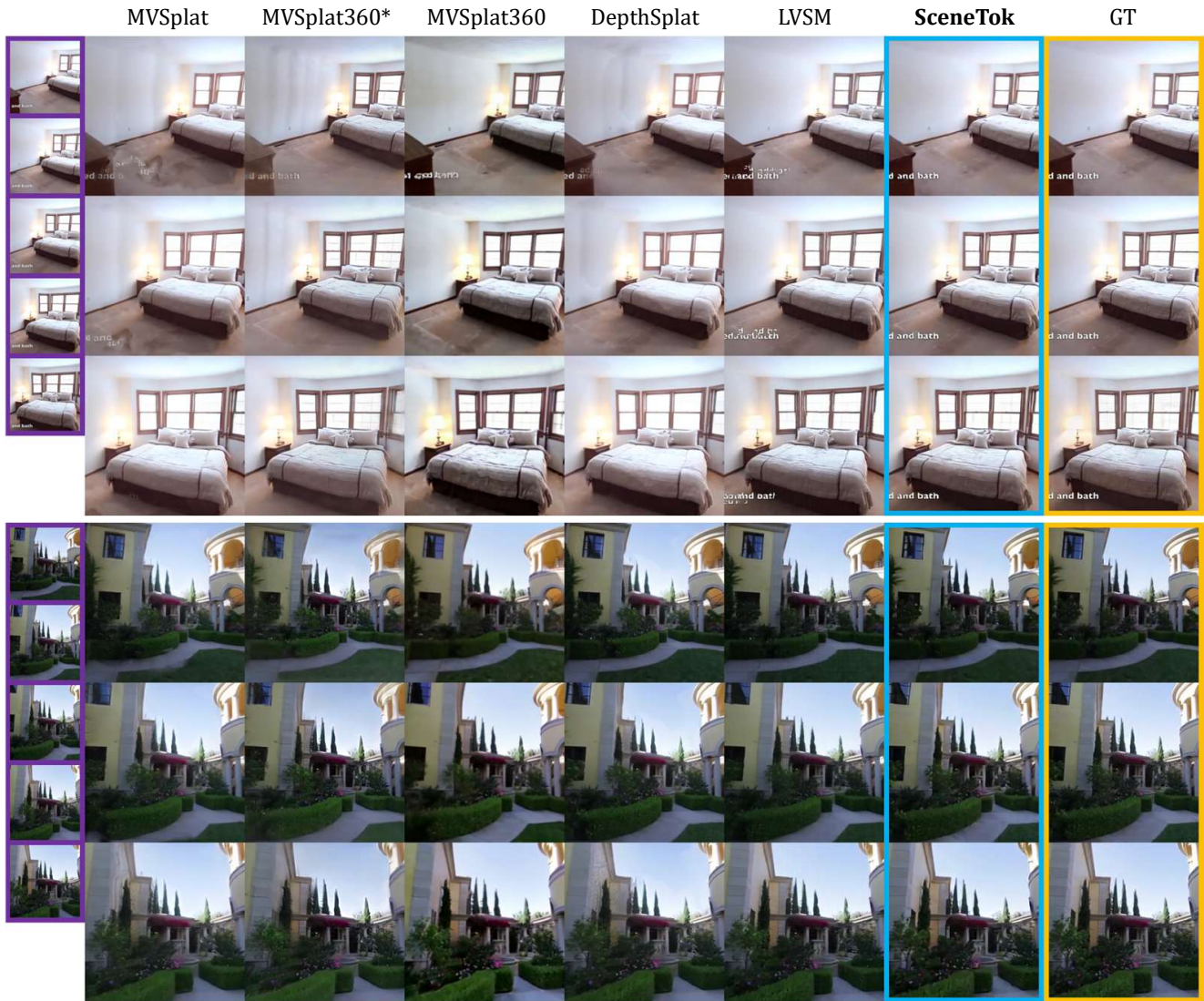


Figure 19. **Qualitative NVS on RealEstate10K.** (□, □, □) denotes the 5 input context views, the target renderings from SceneTok and the corresponding ground-truth target views respectively (we show six views from top-to-bottom). \* denotes output of MVSplat360 taken before the refinement step with a video diffusion model.

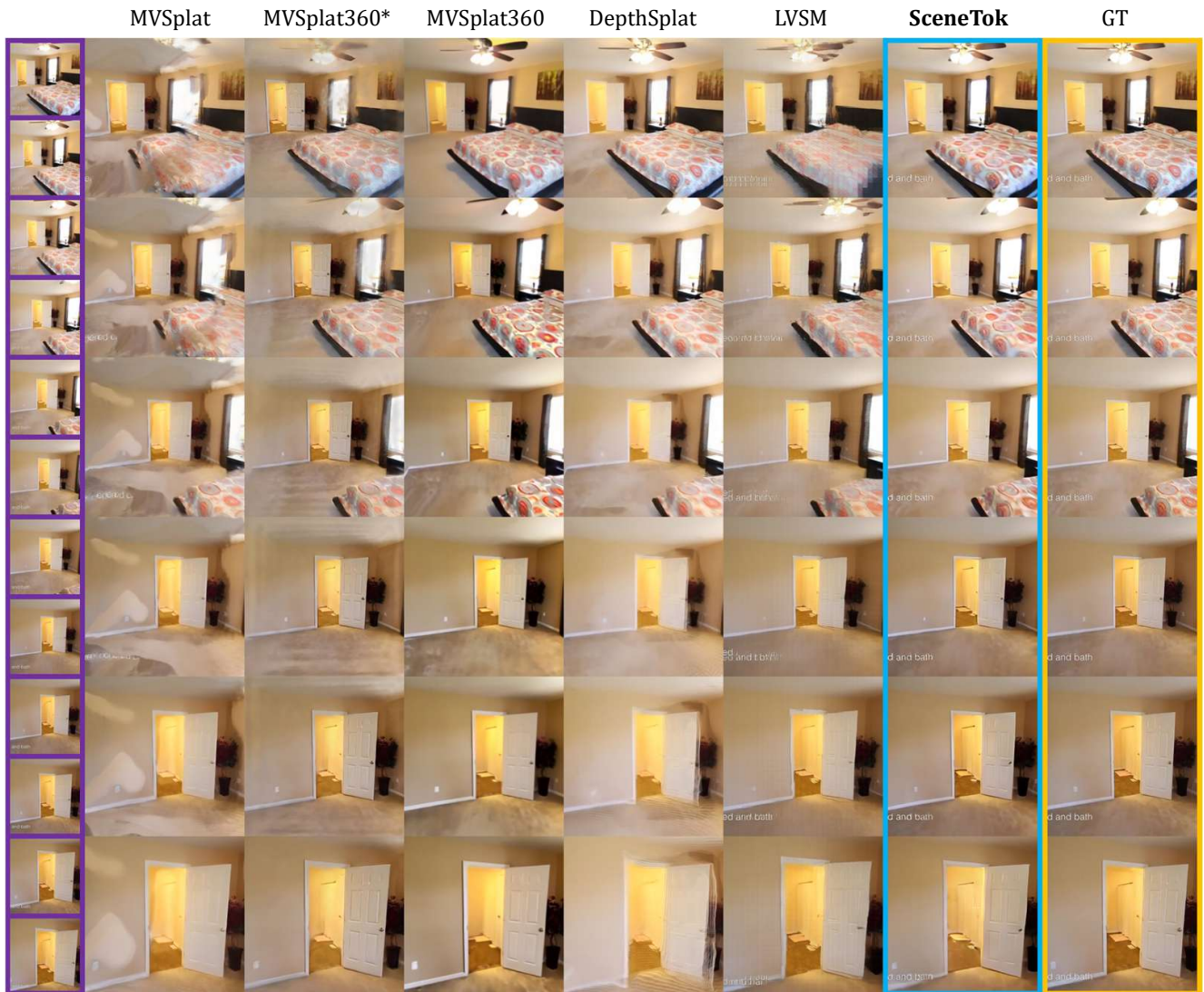


Figure 20. **Qualitative NVS on RealEstate10K.** (□, □, □) denotes the 12 input context views, the target renderings from SceneTok and the corresponding ground-truth target views respectively (we show six views from top-to-bottom). \* denotes output of MVSplat360 taken before the refinement step with a video diffusion model.

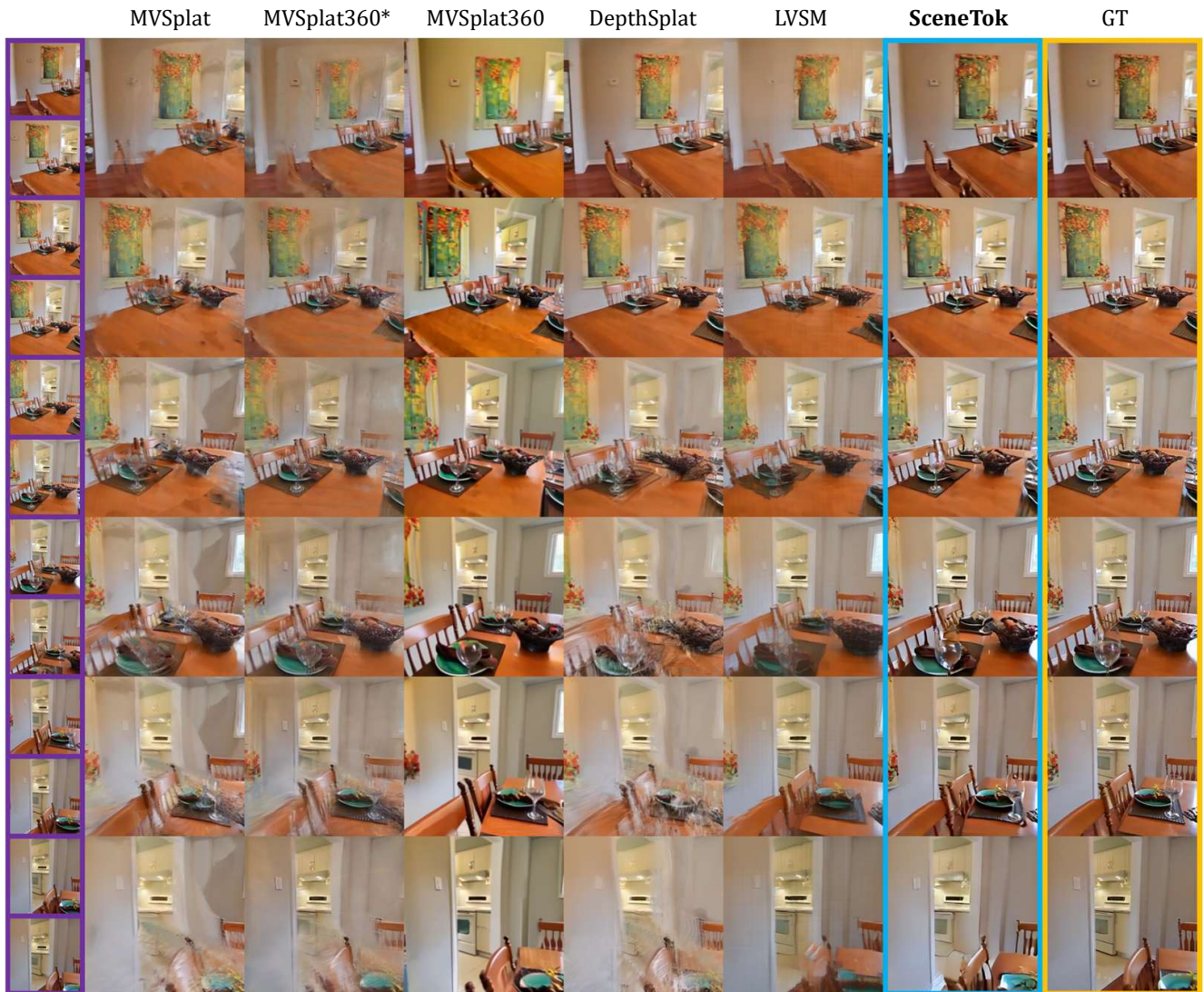


Figure 21. **Qualitative NVS on RealEstate10K.** (□, □, □) denotes the 12 input context views, the target renderings from SceneTok and the corresponding ground-truth target views respectively (we show six views from top-to-bottom). \* denotes output of MVSplat360 taken before the refinement step with a video diffusion model.

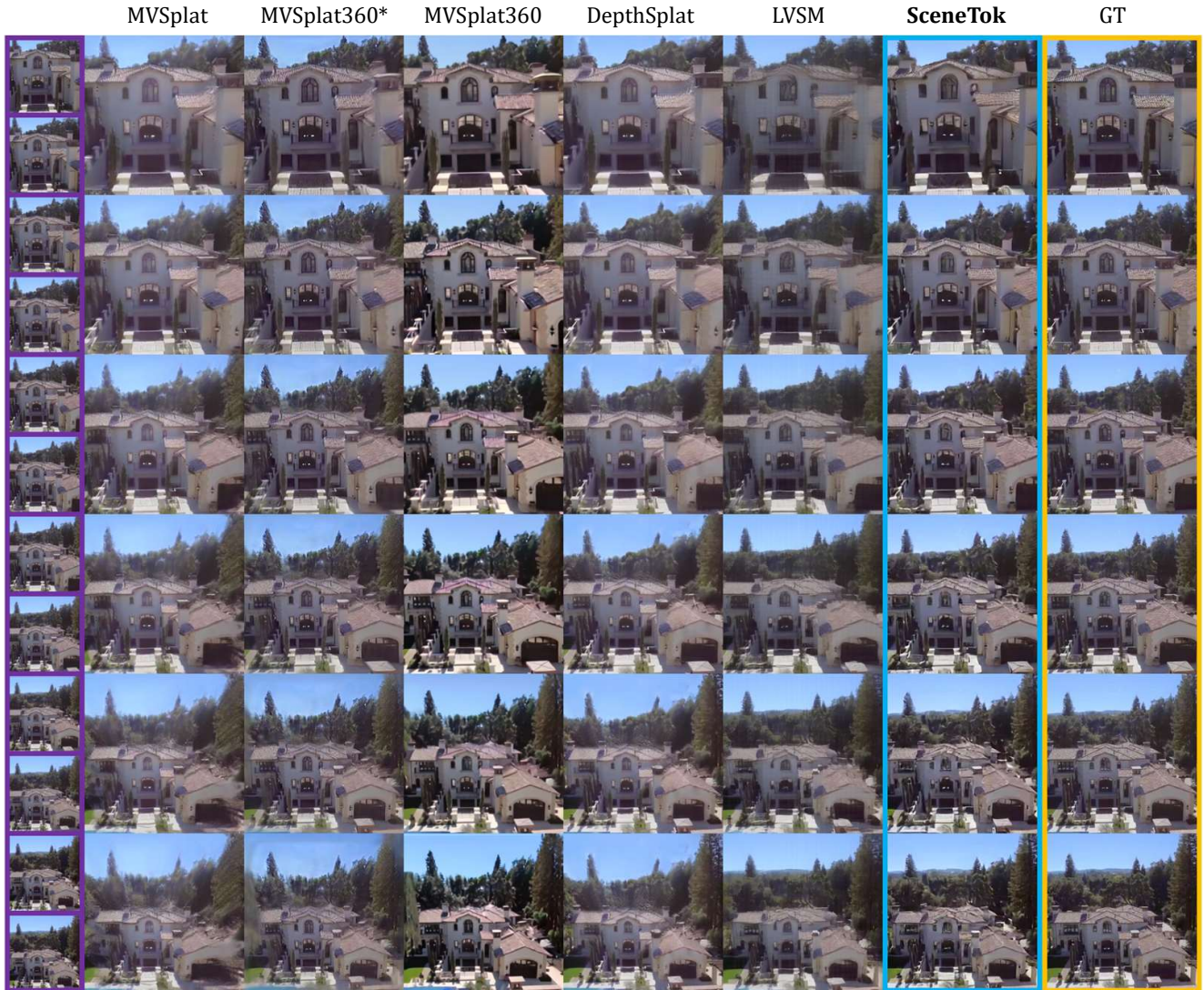


Figure 22. **Qualitative NVS on RealEstate10K.** ( ) denotes the 12 input context views, the target renderings from SceneTok and the corresponding ground-truth target views respectively (we show six views from top-to-bottom). \* denotes output of MVSplat360 taken before the refinement step with a video diffusion model.

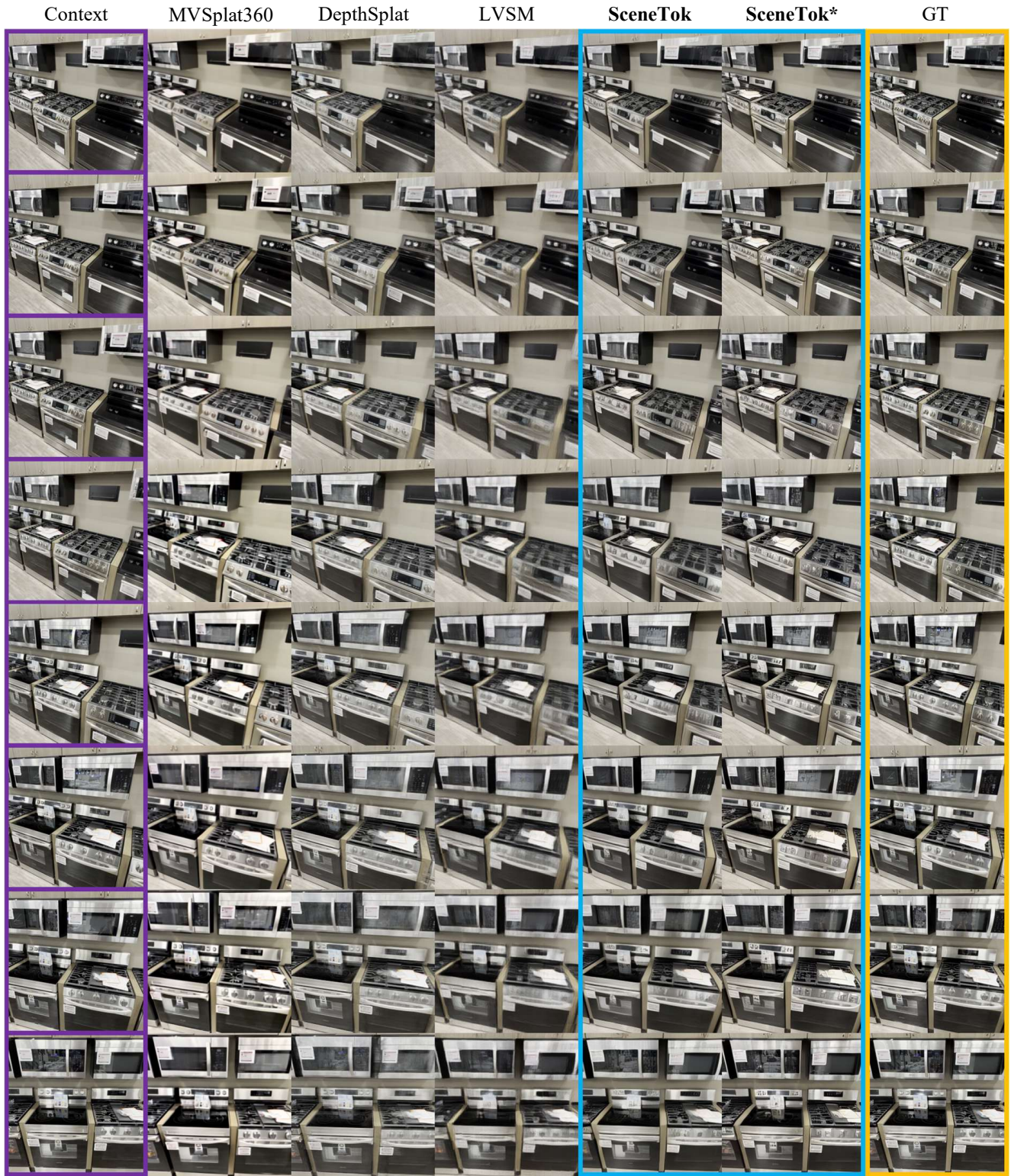


Figure 23. **Qualitative NVS on DL3DV-140.** (□, □, □) denotes the input context views (only 8 are shown), the target renderings from SceneTok (\* denote decoder version trained with WanVAE [50]) and the corresponding ground-truth target views respectively (we show eight views from top-to-bottom).



Figure 24. **Qualitative NVS on DL3DV-140.** (□, □, □) denotes the input context views (only 8 are shown), the target renderings from SceneTok (\* denote decoder version trained with WanVAE [50]) and the corresponding ground-truth target views respectively (we show eight views from top-to-bottom).



Figure 25. **Qualitative NVS on DL3DV-140.** (□, □, □) denotes the input context views (only 8 are shown), the target renderings from SceneTok (\* denote decoder version trained with WanVAE [50]) and the corresponding ground-truth target views respectively (we show eight views from top-to-bottom).

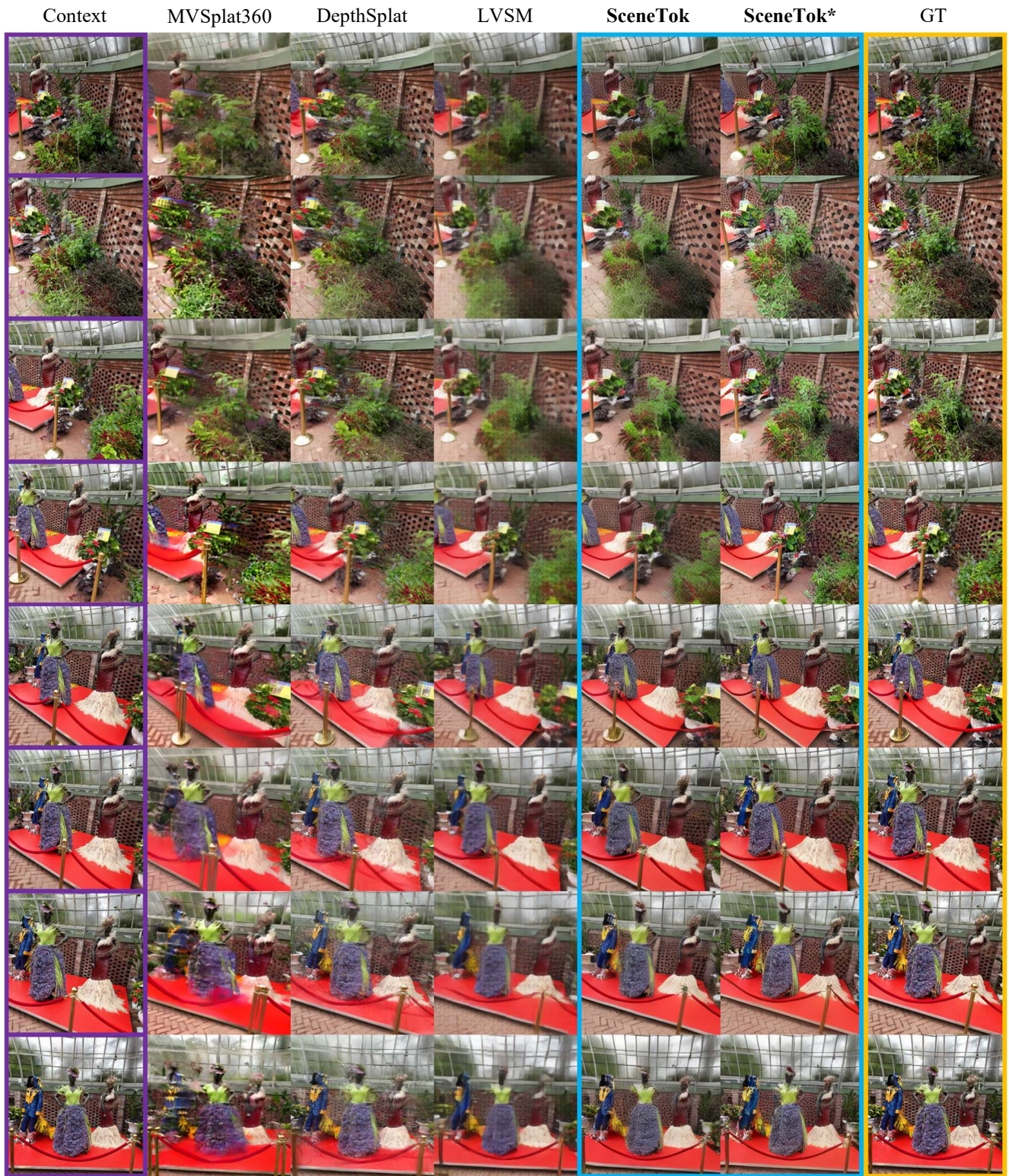


Figure 26. **Qualitative NVS on DL3DV-140.** (□, □, □) denotes the input context views (only 8 are shown), the target renderings from SceneTok (\* denote decoder version trained with WanVAE [50]) and the corresponding ground-truth target views respectively (we show eight views from top-to-bottom).

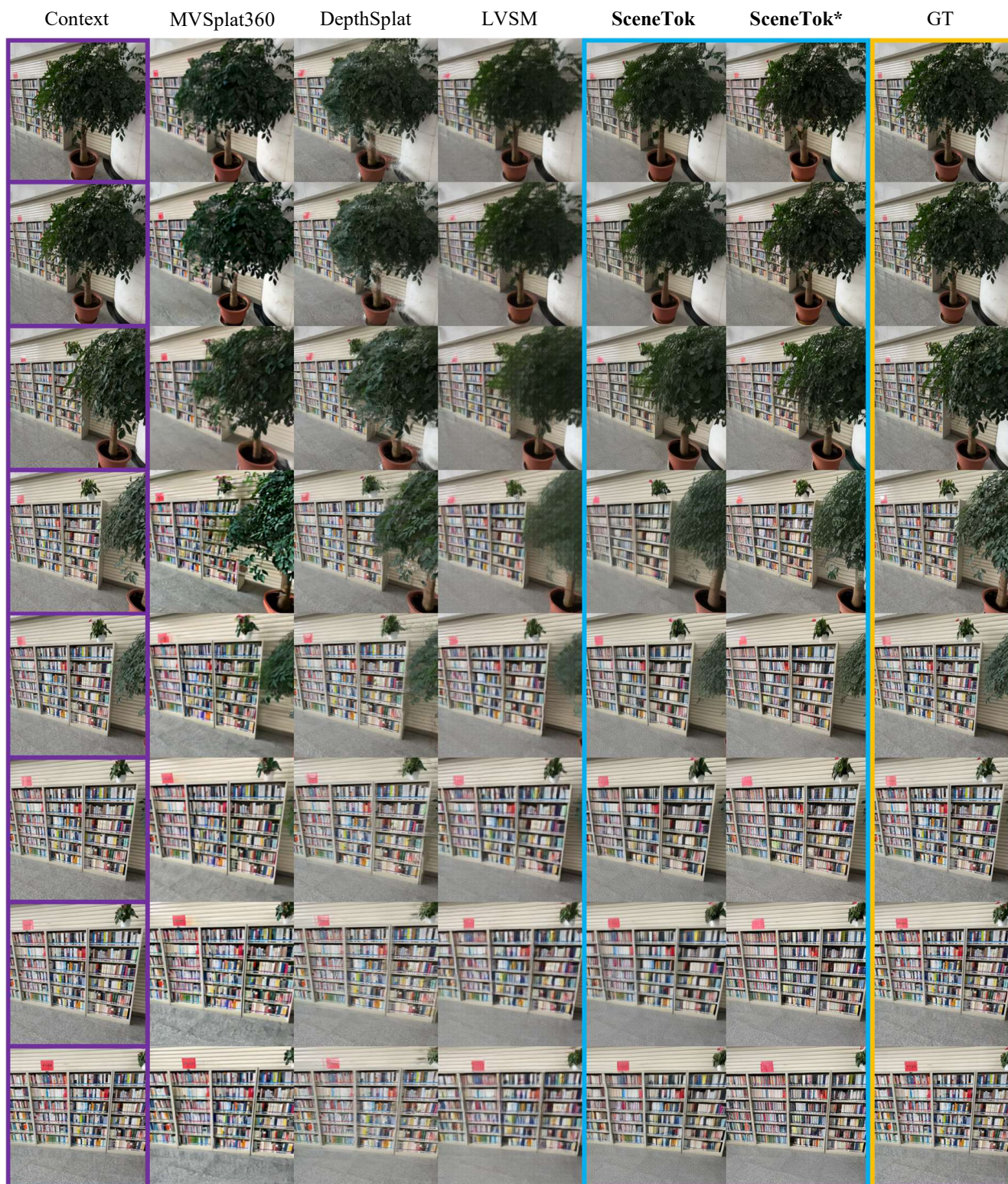


Figure 27. **Qualitative NVS on DL3DV-140.** (□, □, □) denotes the input context views (only 8 are shown), the target renderings from SceneTok (\* denote decoder version trained with WanVAE [50]) and the corresponding ground-truth target views respectively (we show eight views from top-to-bottom).



Figure 28. **Qualitative NVS on DL3DV-140.** (□, □, □) denotes the input context views (only 8 are shown), the target renderings from SceneTok (\* denote decoder version trained with WanVAE [50]) and the corresponding ground-truth target views respectively (we show eight views from top-to-bottom).

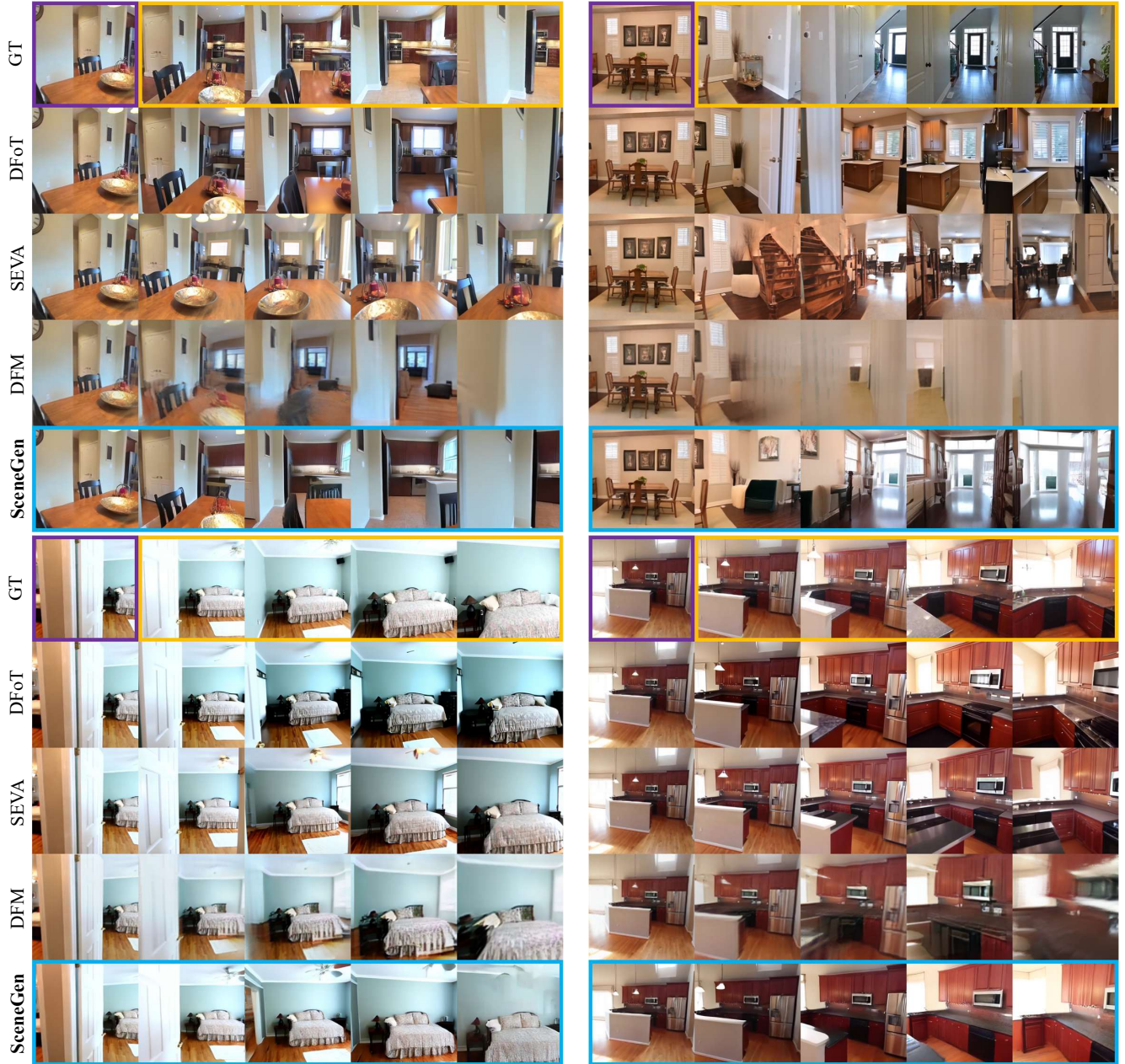


Figure 29. **Qualitative Single-View Generation Comparison.** (□, □, □) denotes the input view, the target renderings from SceneGen and the corresponding ground-truth target views respectively.

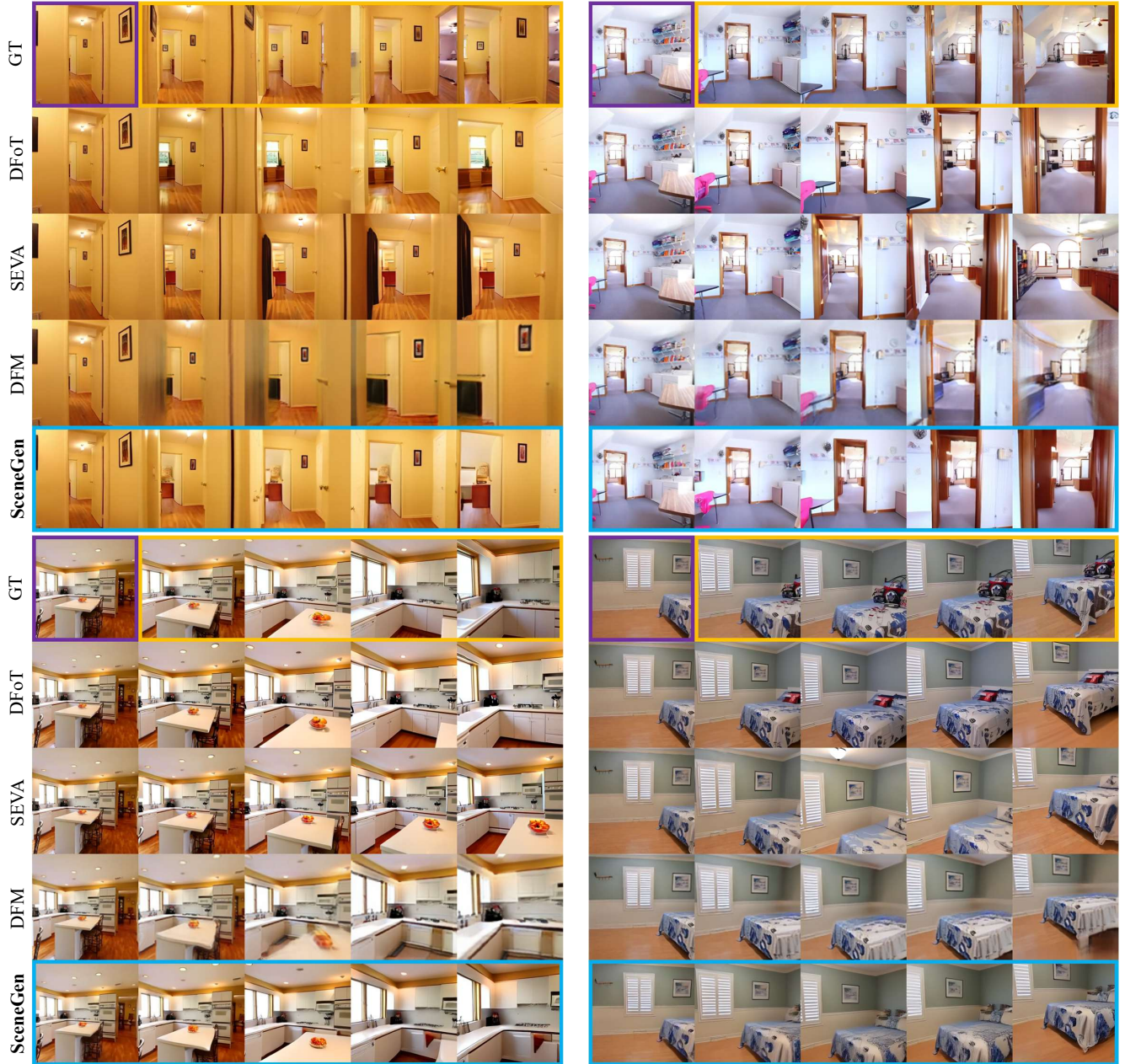


Figure 30. **Qualitative Single-View Generation Comparison.** (□, □, □) denotes the input view, the target renderings from SceneGen and the corresponding ground-truth target views respectively.